Optical Coherence Imaging of Biological Tissues

Risma Job

A Dissertation Submitted to
Indian Institute of Technology Hyderabad
In Partial Fulfillment of the Requirements for
The Degree of Master of Technology

Department of Biomedical Engineering

June, 2015

Declaration

I declare that this written submission represents my ideas in my own words, and where others' ideas or words have been included, I have adequately cited and referenced the original sources. I also declare that I have adhered to all principles of academic honesty and integrity and have not misrepresented or fabricated or falsified any idea/data/fact/source in my submission. I understand that any violation of the above will be a cause for disciplinary action by the Institute and can also evoke penal action from the sources that have thus not been properly cited, or from whom proper permission has not been taken when needed.

(Signature)

RISMA JOB

(– Student Name –)

BM13M1004

(Roll No)

Approval Sheet

This thesis entitled "Optical Coherence Imaging of Biological Tissues" by Risma Job is approved for the degree of Master of Technology from IIT Hyderabad.

Dr. Vandana Sharma

Examiner

Dr. Renu John
Associate Professor and Head
Department of Biomedical Engineering
Indian Institute of Technology, Hyderabad

Adviser

Dr. Harikrishnan Unni

Chairman

Acknowledgements

I am very grateful to my supervisor Dr. Renu John, Department of Biomedical Engineering, IIT Hyderabad, for his encouragement, valuable suggestions, and guidance throughout the project.

I am also thankful to the PhD scholars, Vimal Prabhu and Praveen Kumar, and the other members of Biomedical Optics lab for their assistance and support.

Finally, I would like to thank all my friends and family members for their continual support throughout the course of my studies.

Abstract

Optical Coherence Tomography (OCT) is an emerging technology that has been successfully demonstrated as a potential diagnostic tool. Non-invasiveness, non-contact imaging and *in vivo* imaging capabilities, 3-D structural visualization, and cellular resolution are few of the features that make OCT attractive to the researchers and the medical community. This thesis discusses the development of a Spectral domain OCT system for the imaging of biological tissues. Computational image reconstruction was performed on raw OCT data from the system to produce images of the tissues with high quality. OCT imaging was further explored for the imaging of nanostructural alterations in tissues. This was carried out using the recently developed technique called nanosensitive-OCT, by which it is possible to extend the sensitivity of OCT imaging down to nanoscales. This is performed by mapping the energy contribution of axial spatial frequency sub-bands to each voxel of a 3-D OCT image, and thereby finding the dominant axial spatial periods, which corresponds to the dominant axial structural sizes. Detection of such nanoscale changes in tissues can have promising applications in early cancer diagnosis, where such changes in cell nucleus are markers of carcinogenesis. The fact that imaging can be performed *in vivo* makes it much superior to conventional microscopy techniques in that it is cheaper and can easily be translated into clinical use.

Nomenclature

λ	Wavelength
k	Wave number
E_i	Electric field of the incident wave
E_R	Electric field of the reference beam
E_S	Electric field of the sample beam
Δz	Axial resolution
Δx	Lateral resolution
ϕ	Phase
n	Refractive index
$\mathbf{K}$	Scattering wave vector
ν_x, ν_y, ν_z	Spatial frequencies in the x,y,z directions
H_{zl}	Axial spatial period
OCT	Optical Coherence Tomography
SESF	Spectral Encoding of Spatial Frequency
Ns-OCT	Nanosensitive OCT
ISAM	Interferometric Synthetic Aperture Microscopy
LSS	Light Scattering Spectroscopy

List of Figures

Contents

Chapter 1

Introduction and Background

1.1 Imaging of biological tissues

Imaging of biological tissues is essential for the diagnosis, monitoring and management of diseases. They can also serve as a tool to understand better about the disease pathogenesis, thereby leading to the development of new therapeutics. This has led to the rise of many biomedical imaging technologies which have made clinical analysis and medical interventions possible.

Traditionally, the main form of imaging was direct visualization by dissection. Imaging of the internal structures of the body without dissection began with the discovery of X-rays by Wilhelm Rontgen in the late 1800's. Over many decades, several improvements in this technique have resulted in a great progress in the quality of images produced. In the early 1940's ultrasound technology entered the medical field and has wide variety of applications in real time imaging. Computed tomography was a revolutionizing technology that came into being in the early 1970's, invented by Godfrey Hounsfield. Following the CT scanner came the MRI (Magnetic Resonance Imaging), with tremendous applications in soft tissue imaging. Since then, a lot of researchers have been involved in innovations in magnetic resonance imaging. Functional imaging was introduced through nuclear imaging systems such as PET (Positron Emission Tomography) and SPECT, which provides functional characterization of tissues. PET/MRI and PET/CT technologies are widely being used diagnostic tools, especially with applications in oncology. At the same time, tools for cellular imaging, i.e., microscopy, had been advancing over the years from the ancient simple microscopes, through compound microscopes, to modern day high magnification optical, electron, and scanning probe microscopes[1].

1.2 OCT as a biomedical imaging technology

Optical coherence tomography (OCT)[2] is an interferometric imaging technique that employs near-infrared light to non-invasively image samples, particularly biological tissues. It can image depths upto few millimeters into the sample with micron scale axial resolution. It provides a way of cross-sectional imaging of tissue microstructure *in vivo*. It was invented in 1991[2], and since then, the implementation of the technique has evolved a lot, from the early time-domain implementation to spectral-domain. Its provides resolutions of 1-15 μm, which is much finer than conventional ultrasound. These unique features make it a promising imaging technology for research and clinical applications. OCT is of particular interest to the medical community because of the fact that it provides tissue images at resolutions much better than most other non-invasive 3D imaging modalities, such as CT (computed tomography), MRI, and ultrasound, making it suitable for *in vivo* analysis at near histological resolutions.

Non-invasive imaging of tissue morphology with cellular resolution could provide a lot of clinical advantages with respect to early diagnosis, understanding of disease pathogenesis, and treatment monitoring. OCT is one such imaging modality that provides 'optical biopsy' in real time. It can be described so, because of its ability to image tissue samples with resolutions approaching that of histology, but without tissue excision and processing[3, 4]. In this regard, OCT finds a lot of applications in several clinical situations such as: (1) where conventional excisional biopsy is not possible; examples being eyes, nervous tissue, and arteries (2) where there is chance of sampling error due to standard excisional biopsy missing the lesion. In such cases, OCT can be used to guide biopsy to minimize sampling errors and improve sensitivity. (3) As an image guidance tool in interventional procedures. This medical imaging modality has had a huge impact in the field of ophthalmology. OCT has also expanded its horizon into various other biological applications including gastroenterology, cardiology, tumour margin demarcation, etc. A lot of research is going on in OCT with the objectives of improving resolution, increasing data acquisition speed, optimizing tissue penetration, and contrast enhancement[5].

OCT imaging follows the same principle as that of ultrasound imaging, with the difference being that, it employs light instead of sound. It measures the magnitude and echo time delay of backscattered light in order to generate images. An optical beam incident into the tissue will get backscattered differently from the various structures due to their different optical properties. The echo time delays taken for the light to return from different axial distances can be used to determine the dimensions of these structures. The incident beam is scanned transversely and

multiple axial measurements of echo time delay (axial scans or A-scans) are taken to generate cross-sectional images. The two-dimensional data set representing the optical backscattering in a cross-sectional plane is termed as a B scan. Volumetric three-dimensional information is acquired by scanning the incident optical beam in a raster pattern.

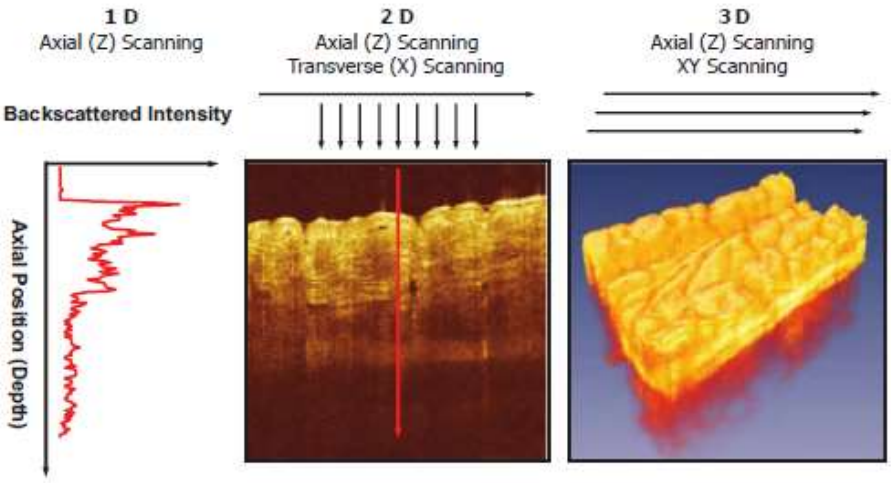

Figure 1.1: Axial scans (A-scans) measure the backreflection versus depth. Cross-sectional images (B-scan) are generated by performing a series of axial scans at different transverse positions. Three-dimensional data sets (3D-OCT) can be generated by raster scanning the sample

The very first clinical application of OCT was in the imagery of eye, it being a transparent tissue. The technology has helped the ophthalmologists greatly with regard to disease diagnosis and monitoring of the eyes. The use of longer optical wavelengths enabled the use of OCT in the imaging of non-transparent tissues. At longer wavelengths of 1300 nm, optical scattering is reduced and about 2-3mm of penetration depths is achieved. This enables the detection of many disease pathologies as the diagnostic changes in tissue morphology usually occur at such depths (especially at the epithelial surface).

Detection of early stage cancers, through identification of early neoplastic changes in the tissue is one of the major potential clinical applications of OCT. Neoplastic changes involve changes in architectural morphology and tissue organization and they fall within the resolution limits of the OCT systems. Many in vitro studies have investigated OCT's ability to diagnose early cancers in several tissues such as gastrointestinal, respiratory, urinary and gynecology [6-9]. Various *in vivo* studies have also been reported in animals and humans [10-13] .

As mentioned earlier, OCT can guide surgical interventions. Since it has the ability to view sub-surface features of tissue *in vivo*, it can be exploited to guide surgery near delicate structures such as nerves and blood vessels, and aid in microsurgical procedures [14-18]. OCT can be utilized in surgical procedures in the form of handheld OCT probes or integrated with surgical microscopes.

For *in vivo* OCT imaging of tissues of internal organs, it is essential to develop internal body imaging systems. OCT has the advantage that it can be easily integrated with existing medical instruments such as laparoscopes, endoscopes, catheters and handheld surgical probes, enabling internal body imaging[19].

In short, the following features of OCT has made it an attractive imaging technology for biomedical applications:

1. High resolutions, much better than conventional ultrasound. This enables imaging of tissues with cellular resolution, almost comparable to that of histology.
2. Non-invasive, *in vivo* imaging is possible unlike microscopy, where imaging is performed on excised tissues.
3. Real time imaging is possible as it does not require any tissue preparation like in histopathology, where significant time and effort is lost in tissue excision and post processing.
4. Being a optical fibre-based technology, it can be easily integrated to a large variety of different instruments, thus widening its applications to internal body imaging
5. OCT devices can be made compact and portable, which makes it a very easy-to-handle technology for physicians.

1.3 Comparison with other imaging modalities

The various imaging modalities can be compared on the basis of parameters such as resolution, imaging depth, image acquisition time, complexity etc. Figure 1.2: A comparison of resolution and imaging depths of OCT to other imaging modalities clearly depicts where OCT stands in terms of resolution and imaging depth. OCT has imaging depth limited to a few millimeters, which is less compared to MRI, CT and ultrasound, but has a much superior resolution. The resolution of ultrasound imaging depends on the frequency used and it is typically about 0.1-1 mm. High frequency ultrasound of ~100 MHz provides resolutions of 15-20 μm, but such high frequencies suffer strong attenuation in tissues which limits the imaging depth to few millimeters.

OCT is often compared with confocal microscopy, which has an extremely high resolution approaching 1µm. but its imaging capability is restricted to a few hundred microns in biological tissues. OCT thereby, fills the gap between microscopy and ultrasound imaging. As mentioned earlier, OCT provides an axial resolution of 1- 15 µm, which is one to two orders of magnitude higher than that provided by ultrasound imaging. The principal limitation of OCT is that it cannot image beyond depths of ~2 mm as light is strongly scattered by most tissues.

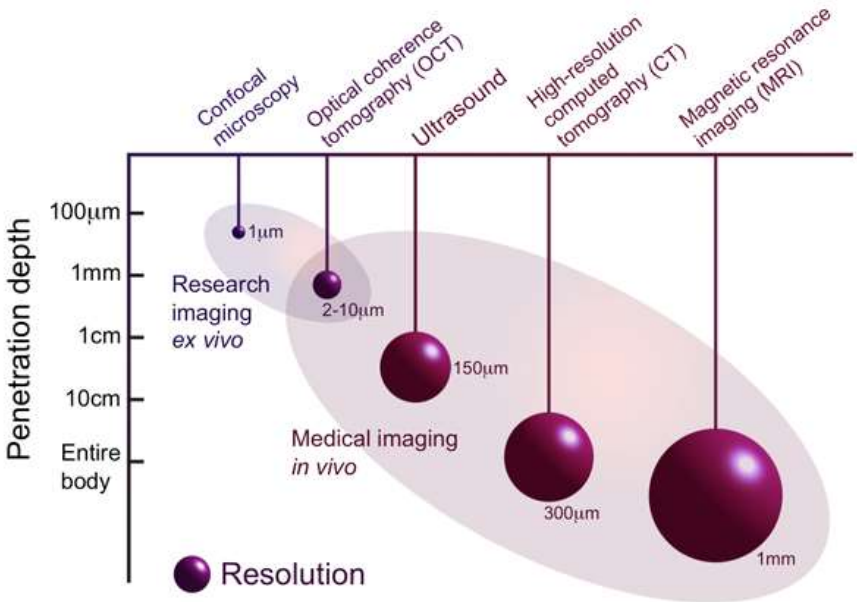

Figure 1.2: A comparison of resolution and imaging depths of OCT to other imaging modalities

1.4 History of OCT

Huang et al. first demonstrated imaging by OCT in the year 1991[2]. When it was first introduced, it was mainly applied to study the eye *in vivo* and evaluate any defects in the retinal layers and optic disc [20-22]. Commercial systems for eye OCT providing axial resolutions of ~10 µm began to be widely used by the ophthalmology community.

The early OCT systems were based on a moving reference mirror and it suffered from a scanning speed limitation. In such systems, the intensities of backscattered light from different depths in the tissue sample were obtained by shifting the position of the reference mirror. This particular approach is termed as Time domain OCT (TD-OCT). Various developments have taken place since then, which has led to improved axial resolution[23] and greater speed of scanning[24-26].

The improvement in axial resolution was mainly due to the introduction of broadband light sources into the OCT systems. Axial resolution as high as 2 μm has been reported[27]. Frequency domain approach allowed backscattered light from all tissue depths to be collected simultaneously in a single A-scan without the movement of reference mirror, thus leading to considerable increase in data acquisition speeds [24-26, 28]. The frequency domain approaches are Spectral domain OCT (SD-OCT) and Swept Source OCT (SS-OCT), where the former makes use of a broadband light source, spectrometer and a CCD camera, and the latter uses a narrow bandwidth source swept through a broad range of frequencies and a photodetector. In addition to the speed and resolution improvements, they also offered a high signal-to-noise (SNR) ratio. Volumetric tissue imaging was made possible as huge 3D data sets could now be obtained at a very fast rate, utilizing the frequency domain methods[29, 30]. Presently, most of the clinical OCT systems operate at speeds of about 27000 A-scans/s and axial resolutions of about 5 μm.

1.5 Overview of OCT operation

OCT operates very similar to that of ultrasound imaging, as mentioned earlier. Light is incident on the sample and the time delay and amplitude of backscattered light is measured. Since light travels much faster than sound, measurement by electronic means is not possible; instead, it is achieved by the technique of low coherence interferometry. A Michelson's interferometer configuration is used for this purpose. The set up consists of a low coherence broadband light source which is split into two arms: reference arm and sample arm. The light reflected from the reference arm and the tissue backscattered light from the sample arm is made to interfere and this interference is recorded on a detector. The use of low coherence source means that interference is observed only when the pathlength difference of light in the two arms lies within the coherence length of the light source.

1.5.1 Time domain OCT

Light from the broadband source is split into a sample and reference arm. The reference arm makes use of a reference mirror or reflector to reflect all the light back along the same path. The sample arm focuses the light onto the sample. A cross-sectional image of the tissue sample is obtained by scanning the beam laterally across the sample surface, which is achieved using a sample arm galvanometer mirror. In TD-OCT, during each depth scan, the reference mirror is translated over a range of distance Δz, to obtain an A-scan. This act of axial scanning of the reference mirror accomplishes the optical sectioning of the tissue, as interference is obtained only when the optical

pathlengths of light in the two arms differ by an amount that falls within the coherence length of the light source. The time domain OCT setup in shown in Figure 1.3: TD-OCT setup.

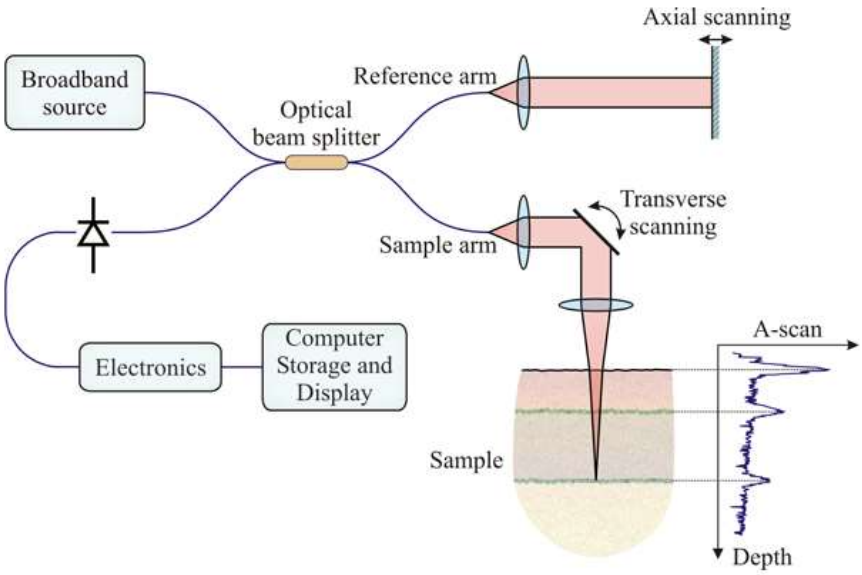

Figure 1.3: TD-OCT setup

1.5.2 Fourier domain OCT

The key difference of FD-OCT from TD-OCT is that the reference mirror is kept stationary. In a single depth scan, all the reflected light from different depths in the tissue are recorded simultaneously. There are two different techniques used in FD-OCT. They are Spectral Domain OCT (SD-OCT) and Swept source OCT (SS-OCT). The former utilizes a spectrometer to analyze the output of the interferometer, and the spectral interferogram is then recorded on the camera. The latter makes use of a frequency tunable laser, which is rapidly swept across a range of frequencies for each sample location, and then recorded on a photodetector. Both techniques record the intensities as a function of wavelength. This data is then Fourier transformed and processed to obtain the reflectivity profile across the depth of the sample. Figure 1.4 illustrates the two methods of Fourier domain OCT operation.

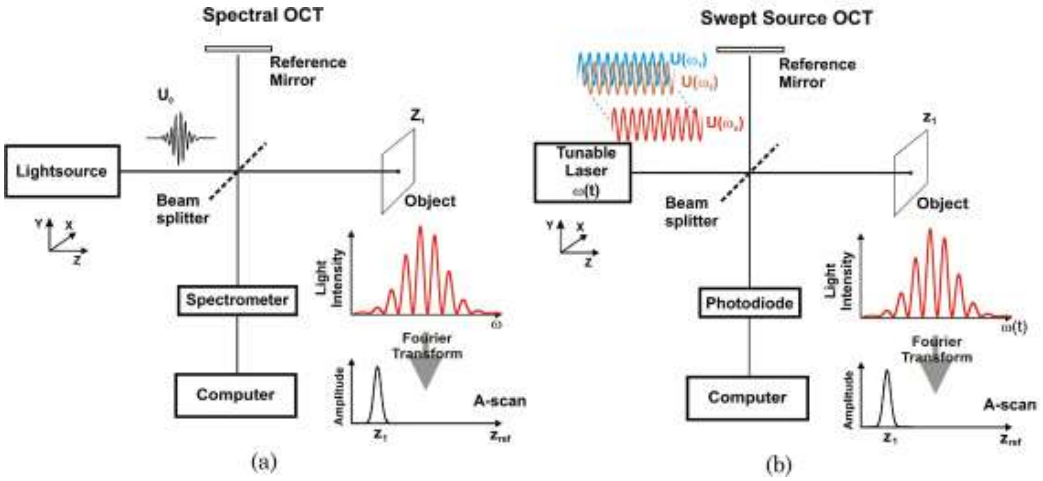

Figure 1.4: Fourier domain OCT set up : (a) Spectral domain OCT (SD-OCT) configuration (b) Swept source OCT (SS-OCT) configuration

1.6 Extensions of OCT

Advances in the field of OCT has led to the development of various functional extensions. These new methodologies are spectroscopic, polarization sensitive, polarization diversity and Doppler flow imaging.

Doppler imaging finds application in determining blood flow in vessels, utilizing the principle that flow causes a Doppler shift in backscattered light, which can be detected by the Fourier transformation of the interference signal. Polarization sensitive OCT detects the changes in polarization state of the light, which arises due to the anisotropic properties of the tissue. This information can be used to map the functional and structural variability in the tissue. Spectroscopic OCT extracts the spectroscopic information about the tissue from the interferometric signal, thus spatially mapping out the spectral absorption and backscattering properties of molecules in the tissue. A relatively recent extension of OCT which images the distribution of magnetic molecular agents in tissue specimen is called Magnetomotive OCT (MM-OCT). It has the capability to detect nanometer scale displacements and can be used to study the tissue's biomechanical properties. The recent developments in the OCT technology has thus enabled new applications.

Chapter 2

Principles of OCT

2.1 Michelson's Interferometer

Michelson's interferometer configuration is the basic structure of an OCT setup. Figure 2.1(a) shows a schematic diagram of a simple Michelson interferometer. The incident light source is divided into two beams, one travelling through the reference arm ($E_R(t)$), and the other through the sample arm ($E_S(t)$), and the beams travel different distances in the two arms of the interferometer. The electric field due to the interference of the two beams is $E_R(t)+E_R(t)$, and the intensity measured by a detector is proportional to the square of the total field:

$$I_0 \sim |E_R|^2 + |E_S|^2 + 2E_R E_S \cos(2k\Delta L) \tag{2.1}$$

where, ΔL is the path length mismatch between the beams in the sample and reference arms. If the reference path length is scanned, interference fringes will be generated as a function of time.

2.2 Low Coherence Interferometry

A very high time resolution is required for the detection of echo time delays of light. To measure distances with a 10 μm resolution, a time resolution of ~30 fs (30×10^{-15} s) is required. This time scale limits the use of direct electronic means of detection and alternative measurement methods such as high-speed optical gating, optical correlation, or interferometry must be used[3].

Therefore, Low-Coherence Interferometry technique is used for the measurement of the magnitude and echo time delay of backscattered light with very high sensitivity [1],[2]. Interferometry

techniques perform correlation or interference between light that is backscattered from the tissue and light that has travelled a known distance or time delay though a reference path. If a coherent (narrow linewidth) light source is used, interference will be observed over a wide range of path length differences. To detect optical echoes, a low-coherence (broad-bandwidth) light source is required. Low-coherence light can be characterized as having statistical phase discontinuities over a distance known as the coherence length, which is inversely proportional to the bandwidth of the light. With low-coherence light, interference is observed only when the path lengths of the reference and measurement arms are matched to within the coherence length of the light. The interferometer effectively measures the field autocorrelation of the light. The magnitude and echo time delay of light can be measured by scanning the reference arm and demodulating the interference signal (Time domain OCT operation). The modulation of the interference signal can be effectively used to determine the magnitude and echo time delay of light.

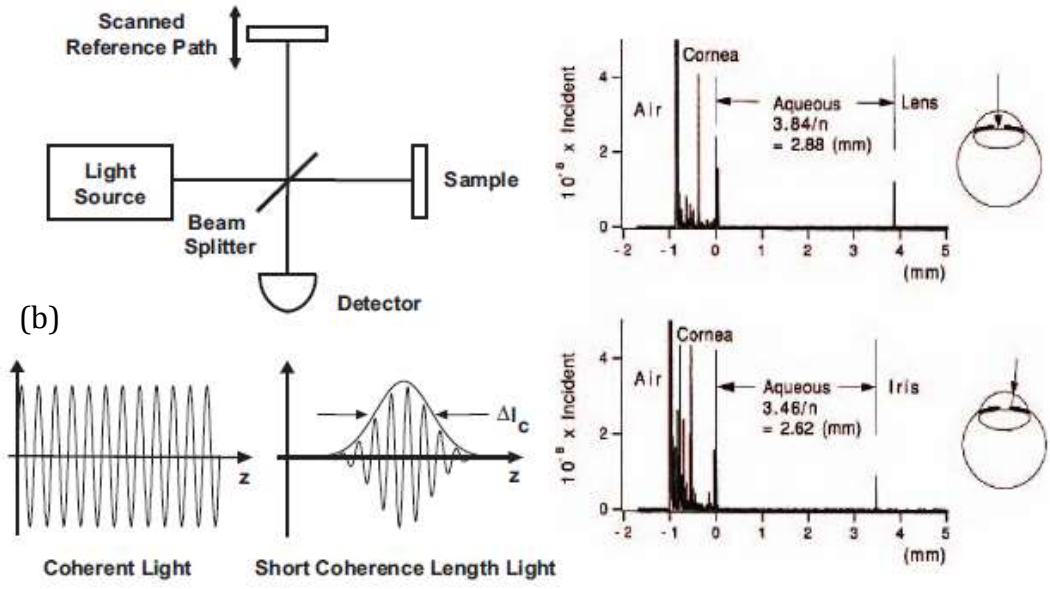

Figure 2.1: (a)Michelson's interferometer, (b) Schematic demonstrating the working of low coherence interferometry.

2.3 Spectral Domain OCT

The basic principles behind SD-OCT are same as that of TD-OCT. But SD-OCT offers high speed advantage due to the absence of mechanical scanning of the reference mirror. Imaging speed as well as signal-to-noise ratio is superior compared to TD-OCT [4]. So it has become indispensable in biomedical imaging applications. It employs a broad-bandwidth light source and the detection of the spectral interferogram is made possible using a spectrometer and a line scan camera. The

Michelson interferometer functions as a spectral filter, which has a periodic output spectrum depending on pathlength mismatch ΔL (shown in Figure 2.2).

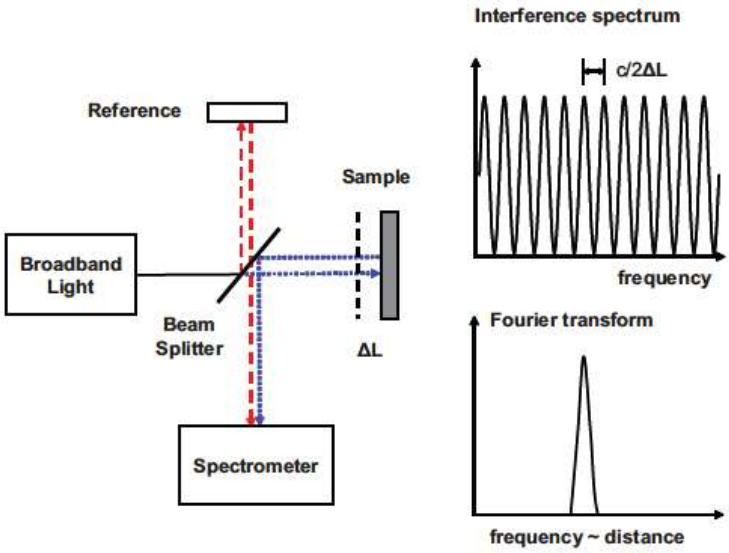

Figure 2.2: A schematic of the working of spectral/Fourier domain OCT detection. Michelson interferometer acts as a periodic frequency filter, the periodicity of which depends on path length mismatch ΔL

Spectrometer measures the interference spectrum, the frequency modulation of which depends on the echo delays. Isolating the interference term,

$$Interference \sim \cos(2k\Delta L)$$

in equation (2.1), we see the dependence of output on two variables; wavenumber k and optical path difference ΔL. The reference mirror in SD-OCT is kept fixed, so ΔL is constant. The interference signal is then a modulation in wavenumber k. This means that, in a single A-scan, the entire depth information is encoded as frequency modulations in the interferogram, thus evading the need for mechanically scanning the reference arm. The axial scan information (echo magnitude and time delay) is obtained by Fourier transforming the output spectrum after conversion from λ-domain to k-domain.

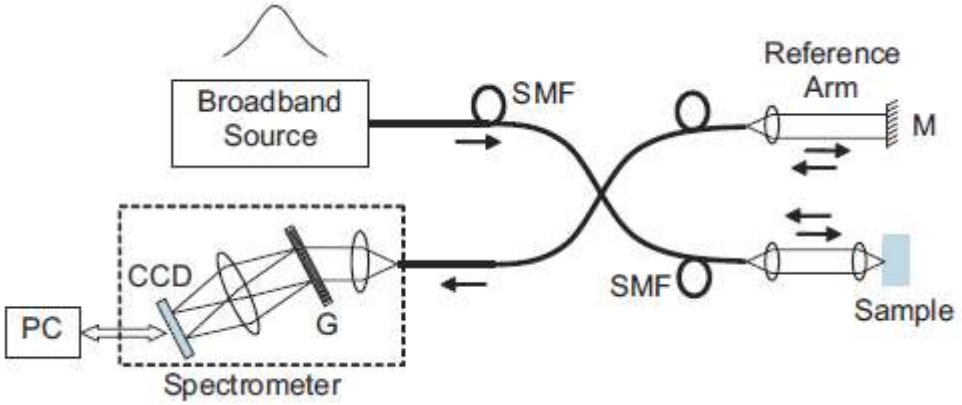

Figure 2.3: A typical SD-OCT Setup

A 50–100 fold increase in imaging speed can be achieved in SD-OCT compared to earlier OCT systems. This high speed advantage can be utilized to increase the number of axial scans per cross-section as well as to increase the number of cross-sectional images acquired in a sequence to yield high definition three-dimensional data (3D-OCT).

2.3.1 Theory of SD-OCT

Consider the Michelson interferometer shown in the Figure 2.4. The broadband light source illuminates the interferometer by a polychromatic plane wave. The electric field of this wave can be expressed as,

$$E_i = s(k,\omega)e^{i(kz-\omega t)} \tag{2.2}$$

where, $s(k,\omega)$ is the spectral distribution of the light source. The beamsplitter BS, with a splitting ratio of 0.5, divides the source beam into the reference and sample arm. The reference mirror is positioned at a distance z_R from the beamsplitter. z_S, on the other hand, denotes the variable pathlength in the sample arm, measured from the beam splitter. Consider that the sample has an electric field reflectivity profile $r_S(z_S)$along the sample beam axis, which can be expressed as

$$r_S(z_S) = \sum_{n=1}^{N} r_{Sn}\delta(z_S - z_{Sn}) \tag{2.3}$$

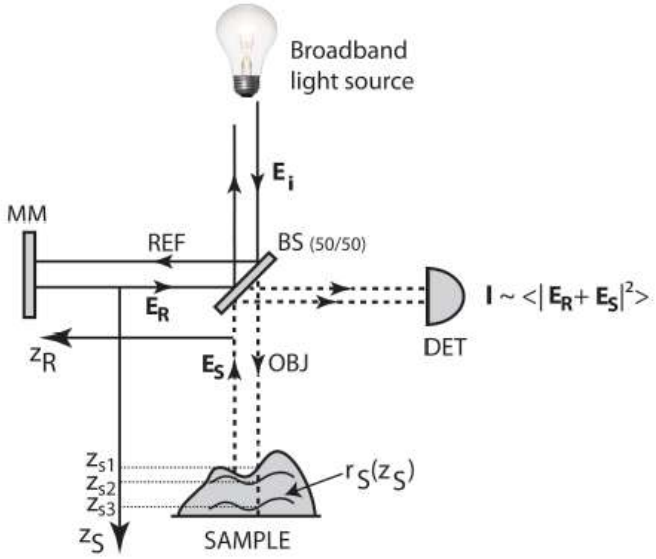

Figure 2.4: Michelson interferometer

Where, r_{Sn} is the field reflectivity at pathlength $z_S = z_{Sn}$. The reflectivity profile $r_S(z_S)$ is assumed to be real and discrete. The power reflectivity of the reflectors is given by $R_{Sn} = |r_{Sn}|^2$. Therefore, we are interested in the general reconstruction of $\sqrt{R_S(z_S)}$.

The electric field of the light beams incident on the beamsplitter, after returning from the reference arm and object arm, E_R and E_S respectively, can be expressed as

$$E_R = \frac{E_i}{\sqrt{2}} r_R e^{i2kz_R} \tag{2.4}$$

$$E_S = \frac{E_i}{\sqrt{2}} \left[r_S(z_S) \otimes e^{i2kz_S} \right] \tag{2.5}$$

where, r_R is the electric field reflectivity of the reference reflector. The factor 2 in the exponentials accounts for the round-trip path length to each reflection and the $1/\sqrt{2}$ factor accounts for the power loss of the light (power gets halved) after passing the beamsplitter the second time. The other half is returned to the light source.

We can now rewrite E_S as,

$$E_S = \frac{E_i}{\sqrt{2}} \sum_{n=1}^{N} r_{Sn} e^{i2kz_{Sn}} \tag{2.6}$$

The reference beam and object beam interfere at the square law detector, generating a photocurrent $I(k,\omega)$ proportional to the square of sum of fields,

$$I(k,\omega)=\frac{\rho}{2}\left\langle\left|E_R+E_S\right|^2\right\rangle=\frac{\rho}{2}\left\langle(E_R+E_S)(E_R+E_S)*\right\rangle \tag{2.7}$$

Where, ρ is the responsivity of the photodetector in Amp/Watt. The angular brackets represent time integration over the response time of the detector. Substituting Equations (2.3) and (2.5) in Equation (2.6) and arbitrarily setting z = 0 yields the following expression for the photocurrent:

$$I(k,\omega)=\frac{\rho}{2}\left\langle\left|\frac{s(k,\omega)}{\sqrt{2}}r_R e^{i(2kz_R-\omega t)}+\frac{s(k,\omega)}{\sqrt{2}}\sum_{n=1}^{N}r_{Sn}e^{i(2kz_{Sn}-\omega t)}\right|^2\right\rangle \tag{2.8}$$

Expanding Equation (2.7) eliminates the terms dependent upon the temporal angular frequency $\omega=2\pi\upsilon$, which is acceptable since υ oscillates at much higher speed than a practical detector can measure. The time invariant photocurrent I(k) becomes,

$$\begin{aligned}I(k)=&\frac{\rho}{4}\left[S(k)(R_R+R_{S1}+R_{S2}+\cdots)\right]\\&+\frac{\rho}{4}\left[S(k)\sum_{n=1}^{N}\sqrt{R_R R_{Sn}}\left(e^{i2k(z_R-z_{Sn})}+e^{-i2k(z_R-z_{Sn})}\right)\right]\\&+\frac{\rho}{4}\left[S(k)\sum_{n\neq m=1}^{N}\sqrt{R_{Sn}R_{Sm}}\left(e^{i2k(z_{Sn}-z_{Sm})}+e^{-i2k(z_{Sn}-z_{Sm})}\right)\right]\end{aligned} \tag{2.9}$$

with $S(k)=\left\langle\left|s(k,\omega)\right|^2\right\rangle$ the light source power spectrum. A Gaussian-shaped spectrum is used to model the light power spectrum $S(k)$. Besides approximately resembling the actual light source spectrum, it has some useful and convenient Fourier transform properties. The inverse Fourier transform (z) of the Gaussian function $S(k)$ is also Gaussian:

$$\gamma(z)=e^{-z^2\Delta k^2}\xleftrightarrow{FT}S(k)=\frac{1}{\Delta k\sqrt{\pi}}e^{-\left[\frac{k-k_0}{\Delta k}\right]^2} \tag{2.10}$$

with k_0 being the central wavenumber of the light source spectrum and Δk its spectral bandwidth, corresponding to the half width of $S(k)$ at $1/e$ of its maximum. The inverse Fourier transform of source spectrum $\gamma(z)$, is referred to as the 'coherence function' and it determines the point spread

function (PSF) of the system. The full width at half maximum (FWHM) of the PSF is the coherence length l_C :

$$l_C = 2\frac{\sqrt{\ell n(2)}}{\Delta k} = \frac{2\ell n(2)}{\pi}\frac{\lambda_0^2}{\Delta\lambda} \tag{2.11}$$

From this definition, we see that the coherence length l_C and the light source bandwidth $\Delta\lambda$ have an inverse relationship, which indicates that a small axial resolution will only be achieved by using a broadband light source. Using Euler's rule to simplify Equation (2.9), we obtain a real result for the photocurrent $I(k)$,

$$\begin{aligned} I(k) = \frac{\rho}{4}\left[S(k)\left(R_R + R_{S1} + R_{S2} + \cdots\right)\right] \\ + \frac{\rho}{4}\left[S(k)\sum_{n=1}^{N}\sqrt{R_R R_{Sn}}\left(\cos\left[2k\left(z_R - z_{Sn}\right)\right]\right)\right] \\ + \frac{\rho}{4}\left[S(k)\sum_{n\neq m=1}^{N}\sqrt{R_{Sn} R_{Sm}}\left(\cos\left[2k\left(z_{Sn} - z_{Sm}\right)\right]\right)\right] \end{aligned} \tag{2.12}$$

Equation (2.12) is commonly referred to as the spectral interferogram, in which we can distinguish three distinct components: the `DC terms', the `Cross-correlation terms' and the `Auto-correlation terms'[3];

1. The DC or constant component which is a path length independent offset to the photocurrent, shaped by the light source power spectrum.
2. The Cross-correlation component describes the interference of the backscattered light from each sample reflector with the light backreflected off from the reference mirror. Their respective path length mismatches z_R - z_{Sn}, impose a frequency modulation of the interference spectrum that contains the depth information for each backscatterer. This is the desired interference signal in OCT.
3. The Auto-correlation terms represent the interference between light backreflected from different sample reflectors and appear in the OCT image as artefacts. By increasing the reference reflectivity R_R, the relative contribution of the Cross-correlation terms will dominate the contribution of the Auto-correlation terms.

2.4 Resolution

Image quality is mainly governed by the resolution of the optical imaging system. OCT is capable of providing axial resolutions of about 1-15 μm, and its axial resolution is independent of the bean focusing and spot size. Since OCT measurement is based on low coherence interferometry, the width of the autocorrelation function determines the axial resolution and it is inversely proportional to the bandwidth of the light source. For a Gaussian spectrum, the axial resolution is given by,

$$\Delta z = \frac{2\ln(2)}{\pi}\frac{\lambda^2}{\Delta\lambda} \tag{2.13}$$

where λ is the central wavelength, Δz is the FWHM (Full Width at Half Maximum) of the autocorrelation function, and $\Delta\lambda$ is the FWHM of the source power spectrum. Because of this inverse relationship between the axial resolution and source bandwidth, high axial resolution is achieved by using broad-bandwidth light sources.

The transverse resolution in OCT is determined by the diffraction limited spot size of the focused beam, similar to that in optical microscopy. The diffraction limited spot size is inversely proportional to the NA (Numerical Aperture) or focusing angle of the beam. The transverse resolution is given by,

$$\Delta x = \frac{4\lambda}{\pi}\frac{f}{d} \tag{2.14}$$

where, f is the focal length and d is the beam spot size.

2.5 Depth of field

From the Eq. (2.14), we can note that by using a large numerical aperture, beam can be focused to a small spot size, and this can be used to achieve fine transverse resolution. But, at the same time, transverse resolution is also related to the depth of field. The imaging depth of field or confocal parameter b, is $2z_R$, or two times the Rayleigh range:

$$b = 2z_R = \frac{\pi\Delta x^2}{\lambda} \tag{2.15}$$

So, there is a trade-off between transverse resolution and depth of field as an increase in transverse resolution causes a decrease in depth of field.

Figure 2.5 shows the two cases of using low NA and high NA focusing, and the corresponding depth of fields. Usually, low NA focusing is performed in OCT systems to obtain a large depth of field. The confocal parameter b, in this case, is larger than the coherence length. However, low NA leads to larger focused spot sizes and hence, low transverse resolution. OCT can also be performed with high NA focusing in order to obtain high transverse resolutions, but it reduces the depth of field to a large extent. This high NA focusing is typically employed in microscopy techniques.

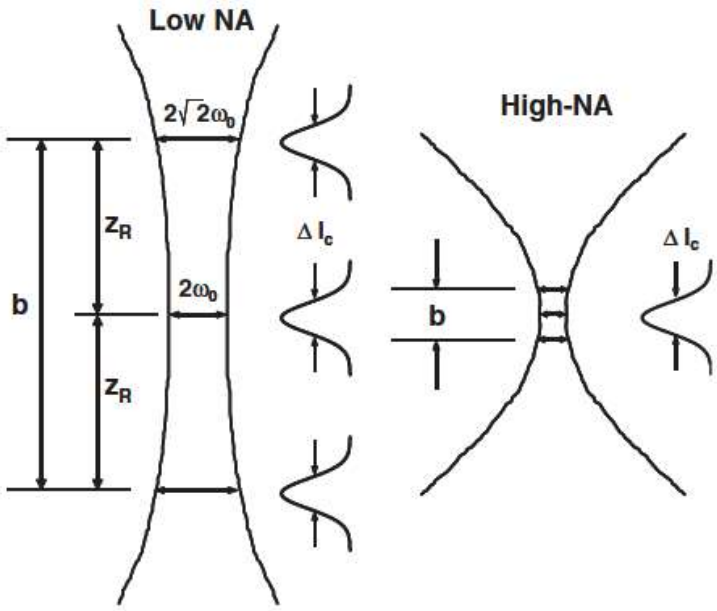

Figure 2.5: High and low NA focusing and the trade-off between the transverse resolution and depth of field.

2.6 Dispersion Effects

Dispersive elements within the OCT system causes the different frequencies in the light beam to propagate with different velocities. An unbalanced dispersion or dispersion mismatch in the two interferometer arms causes the coherence function to broaden, as well as, it decreases its peak intensity[31]. This ultimately results in a loss of depth resolution. Dispersion can be tolerated through hardware modifications such using the appropriate optical components so that the

reference arm and sample arms dispersions are matched. Dispersion compensation can also be achieved through implementation of software algorithms or numerical methods.

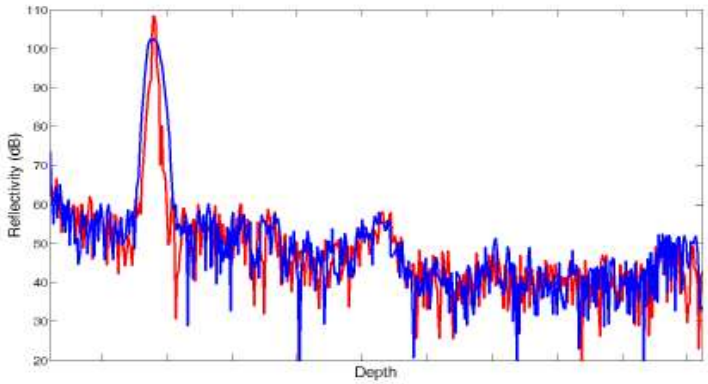

Figure 2.6: Effect of dispersion on the reconstructed axial profile

.

Chapter 3

System Design: Data Acquisition and Control, Spectrometer

3.1 Data Acquisition and control

The quality of the OCT image is highly dependent on the synchronization of all the components in the system, so that image artifacts can be avoided. Transverse scanning of the sample for taking multiple A-scans is carried out by the deflection of the beam by means of the galvanometer actuated mirrors. It is necessary to ensure that the scanning mirrors are stationary while the camera is acquiring an axial scan data, so that the backreflected light can be captured. Otherwise, movement can reduce the number of photons integrated and mixing of signal from nearby positions. So, the scanning of laser beam and the image acquisition by camera should be synchronized to avoid resolution degradation and SNR reduction.

3.1.1 Camera

One of the main components that decides the quality of the spectrometer is the camera.it should have a very good spectral response in the range of source spectrum. The pixel size must be such that it matches the spectrometer's spectral sampling rate. The camera chosen is Basler sprint spL2048-140km line scan camera, and it has two lines of 2048 pixels each. It is interfaced to the computer through a frame grabber. It is capable of working in external trigger and free run modes. The external trigger is carried out via an analog voltage signal and this method is used for

synchronization. Both the frame grabber board and analog output boards for generating the galvanometer control signals were from National Instruments.

3.1.2 Galvanometer control using analog waveform

Scanning is performed by the galvanometer actuated mirror, the movement of which is controlled through an analog voltage waveform applied to its servo driver board. A dual axis control board 673xx (from Cambridge Technologies) was used, where accurate positioning is accomplished by means of feedback of the angular orientation of the galvanometer.

There is a linear relationship between the applied input voltage and the degrees of rotation of the galvanometer, therefore, by giving a ramp or triangular voltage signal in steps, the galvanometer can be made to scan linearly.

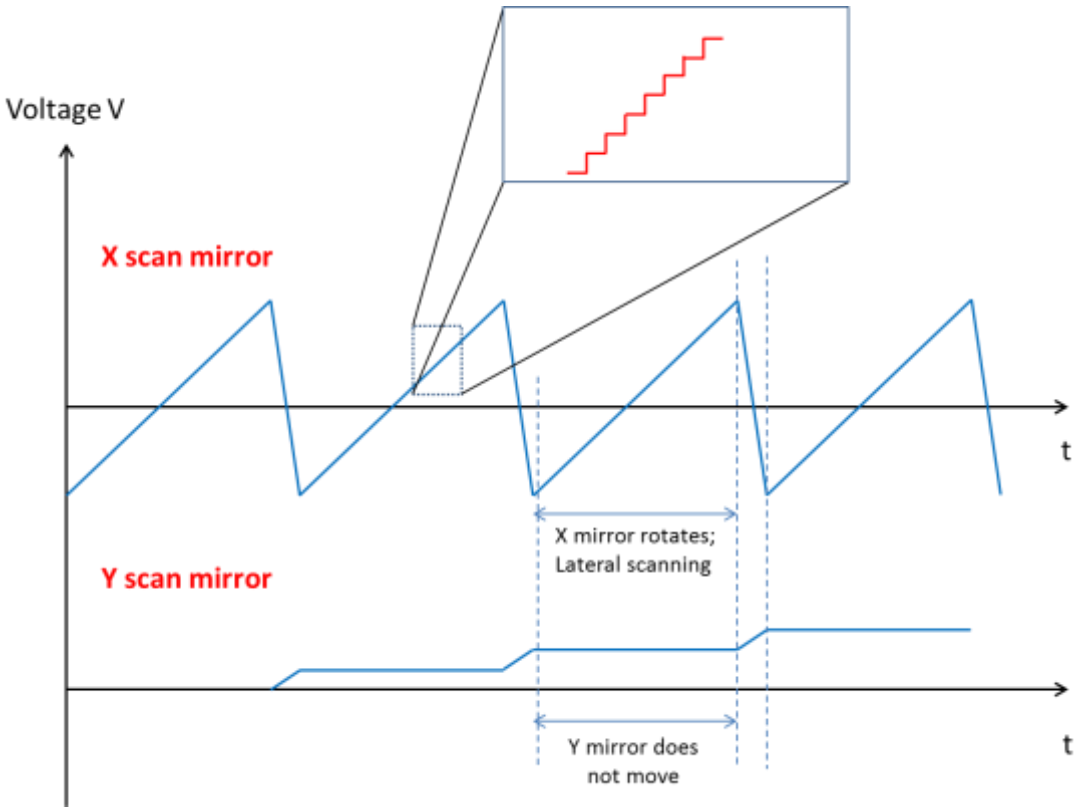

Figure 3.1: The control signals to the galvanometer for x and y scanning

The waveforms input to the two scan mirrors are as shown in Figure 3.1. The x scanning mirror receives a triangular control waveform, where lateral scanning from left to right occurs during the

positive going ramp, and during the negative going ramp, it sweeps fast from right to left. Meanwhile during lateral scanning, the y mirror receives a constant voltage and does not move, whereas during the return of x mirror to the beginning, y mirror receives a voltage change due to which it deflects and the beam moves in the y direction. This is the method by which raster scanning of the sample is achieved, thereby enabling imaging of cross-sections of the sample and eventually, the 3-D data.

3.1.3 Synchronization of image acquisition and scanning

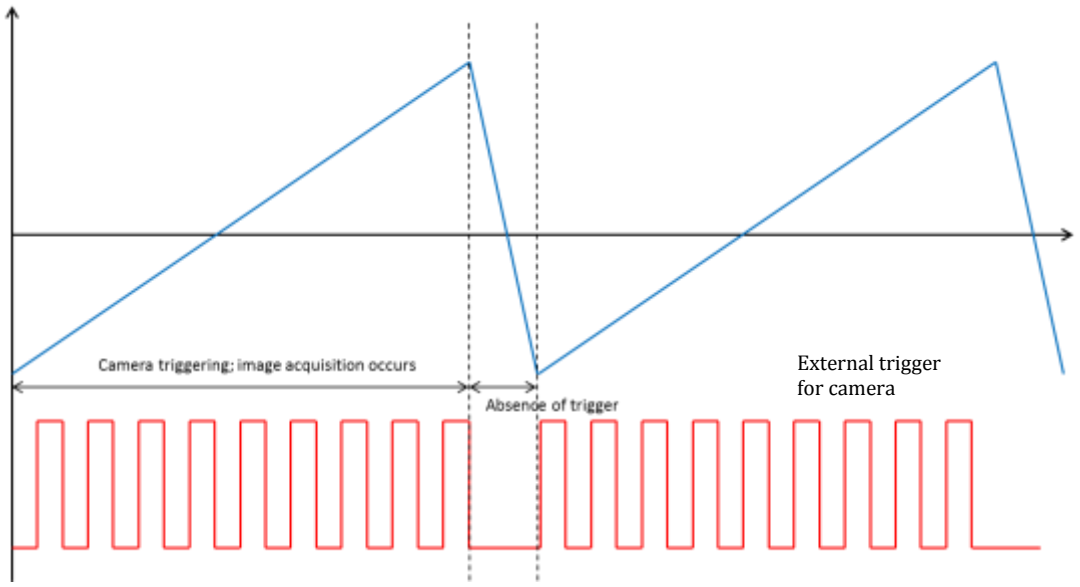

Figure 3.2: The external trigger for camera and its timing with the galvanometer signal

The aim of synchronization between camera and scanning mirrors is to ensure that data/ image acquisition occurs only during the lateral scanning of the beam and not otherwise. From Figure 3.2, the external trigger for camera is timed with the positive going ramp for the x scanning mirror. This synchronization between camera acquisition and scanning is achieved through Labview program, whereby, software methods are used such that the DAQ board outputs the galvo control signals and the camera trigger signals in synchronization. The Figure 3.3 shows how multi-function synchronization is performed through Labview DAQ programming.

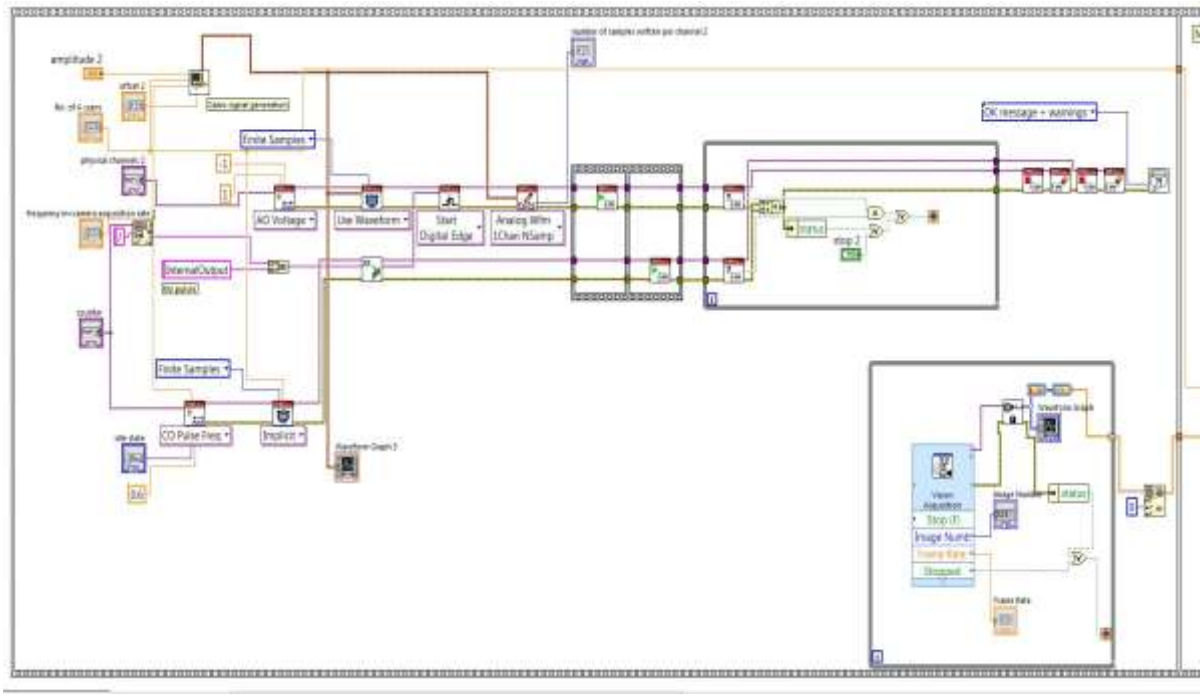

Figure 3.3: A snapshot of the synchronization of image acquisition and beam scanning performed through Labview

3.2 Spectrometer

The key component in a SD-OCT system is the spectrometer. The overall performance and quality of the OCT system relies mainly on it. The widely used configuration of the spectrometer used a grating to separate out the wavelengths, which are then detected by a photodetector, which records the intensity contributions of the different wavelengths in the backscattered light. The axial resolution, sensitivity fall-off and imaging depth are all dependent on the design of the spectrometer. Hence, the main deciding factors dictating the design specifications of the spectrometer are the source spectrum and bandwidth, as well as the required axial resolution and imaging depth.

The four major components of the spectrometer are:

1. The collimation lens
2. Grating
3. Focusing lens
4. Detector

The components are chosen such that they tailor to the specific needs that we require in the SD-OCT system.

As we know, the depth resolution of the OCT systems is limited by the coherence length of the light source,

$$\Delta z = \frac{2\ln(2)}{\pi}\frac{\lambda^2}{\Delta\lambda} \tag{3.1}$$

Where $\Delta\lambda$ – source bandwidth, Δz - full width at half maximum for the depth point spread function.

The light source used for the OCT setup is a Femtosecond laser, which has a central wavelength of 800 nm and a bandwidth of 260 nm. Based on these parameters, the spectrometer specifications are as follows:

Source Bandwidth: 670 – 930 nm

Axial resolution : 1.09 µm

Imaging depth : 1.5 mm

Similar to how the axial resolution is related to the source spectrum bandwidth, the same way the imaging depth $z_{\max}$ is related to the spectral resolution $\delta\lambda$,

$$z_{\max} = \frac{2\ln(2)}{\pi}\frac{\lambda^2}{\delta\lambda} \tag{3.2}$$

Substituting for λ =670 nm, which is the minimum wavelength, the restriction on $\delta\lambda$ is obtained as, $\delta\lambda \leq$ 0.13 nm.

3.2.1 Detector

The spectrometer design begins with the detector, as it is very expensive element and its choice consequently affects the choice of other components. The detector is chosen in such a way that it has a good spectral response in the range of the source spectrum. In order to achieve the calculated maximum spectral resolution of $\delta\lambda \leq$ 0.1 nm and to detect the 260 nm bandwidth, about $260/0.13 \approx 2000$ pixels are required. Out of the commercially available choices of CCD arrays (with 512, 1024, 2048, 4096 pixels), we chose a CCD camera Basler Sprint spL2048-140km with 2048 pixels and 10 µm pitch. Since each pixel is 10 µm x 10 µm with no spacing in between, the resulting array length is 20.48 mm.

3.2.2 Grating

Grating is the dispersive element in the spectrometer. $\delta\lambda$, the spectral resolution of the grating, is related to the diffraction order m and the number of grooves illuminated N as,

$$\frac{\lambda}{\delta\lambda} = mN \tag{3.3}$$

For first order gratings, m is assumed to be 1. To obtain a spectral resolution of $\delta\lambda \leq$ 0.1 nm, and m =1, N should be atleast 9300. Considering a groove density of 1200 lines per mm, the beam diameter should be atleast 7.75 mm, in order to illuminate atleast 9300 grooves. This beam diameter is calculated assuming that the incoming light has a uniform distribution. But, in fibre-based OCT systems, the light travels with a Gaussian profile. For a Gaussian beam distribution, the beam diameter at 1/ε of the maximum is found from the equation,

$$\Delta x_c = \Delta x_{FWHM} \sqrt{\frac{\ln \varepsilon}{\ln 2}} \tag{3.4}$$

After calculations based on the above equation, it if found that the aperture should be atleast 20 mm to collect out to 1% (ε=100) of the maximum. Since the required aperture size is 20 mm, one inch optical components can be used.

The grating that was chosen is a ruled grating from Thorlabs with a groove density of 1200 lines per mm, 750 nm blaze wavelength, $26°44'$ blaze angle and a size of 25mmx25mm.

For a ruled grating, the grating equation is given by,

$$a(\sin\alpha + \sin\beta) = m\lambda\,, \tag{3.5}$$

where α , β are the angles of incidence and diffraction respectively.

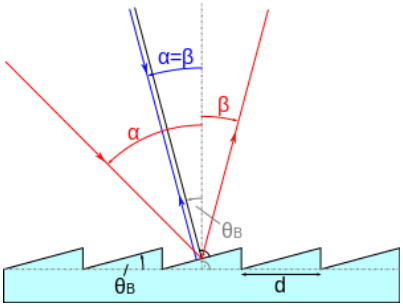

Figure 3.4: Diffraction at a blazed grating

For the Littrow configuration, $\alpha = \beta = \theta_B$, where θ_B is the blaze angle. Then the grating equation becomes,

$$\theta_B = \sin^{-1}\frac{m\lambda}{2a} \tag{3.6}$$

From this, we obtain that the for the central wavelength=800 nm, the optimal efficiency occurs at $\alpha = 30.7°$. Now the angular dispersion for the wavelength range 670-930 nm is calculated from the grating equation. It is found to be around $30.7°$ +/- $10.5°$.

3.2.3 Collimator

We found that a beam diameter of 20 mm is needed to achieve the required spectral resolution. But the beam diameter, in turn depends on the focal length of the collimator and the numerical aperture (NA) of the fibre. The optical fibres used in the set up has an NA of 0.13 nm. The angle at which light exits the fibre depends on the NA by the equation,

$$NA = n\sin(U) \tag{3.7}$$

Taking n=1 for air, and NA=0.13 nm, the angle at which light exits fibre is $\sim 7.5°$. Using the above information, we can calculate and find that the beam reaches a diameter of 20 mm at a distance of $\left(0.5\times\frac{20}{\tan 7.5}\right)\approx 75mm$.

Therefore, the focal length of the collimator is taken to be a 75mm lens.

3.2.4 Focusing optics

The objective of the focusing lens is to focus the dispersed light onto to the detector. the angular spread of the dispersed light is $\Delta\theta = 2\times 10.5°$, and the length of the pixel array L =20.48 mm determines the focal length of the focusing lens as given,

$$F = \frac{L}{2}\div\tan\left(\frac{\Delta\theta}{2}\right)\approx 55mm \tag{3.8}$$

Hence a 55mm lens is used as the focusing optics.

3.2.5 Final Design

Given below is a schematic of the designed spectrometer, where each component was carefully chosen as above. Achromatic doublet lenses are used for collimation and focusing, as it corrects for the chromatic aberrations occurring due to the broadband nature of light.

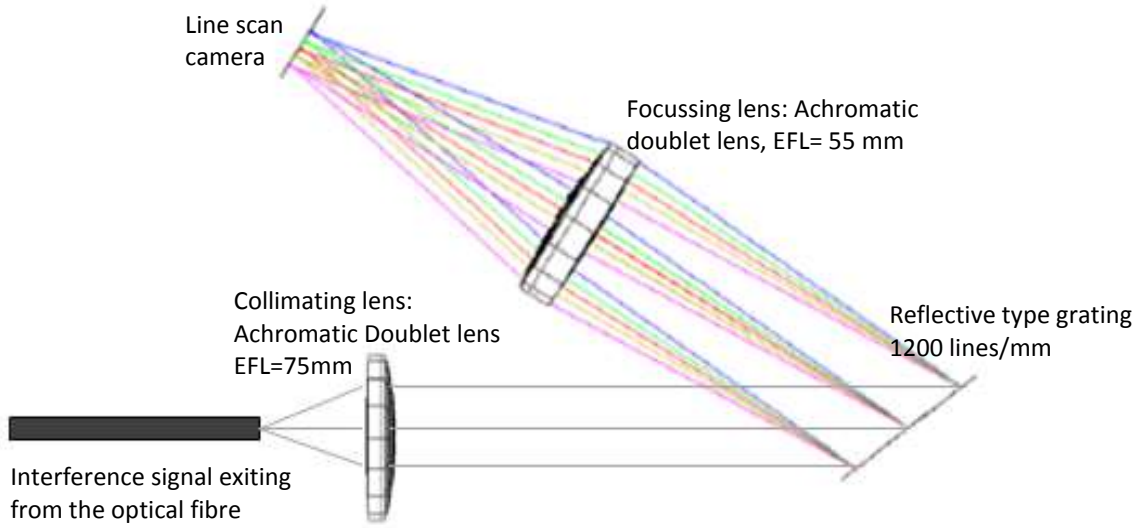

Figure 3.5: Schematic of the spectrometer

Figure 3.6: The spectrometer set-up in lab

3.3 Experimental setup for OCT

A schematic of the OCT setup is shown in Fig. 3.3. My work in the OCT setup was the spectrometer design, programming for galvo mirror scanning and camera synchronization.

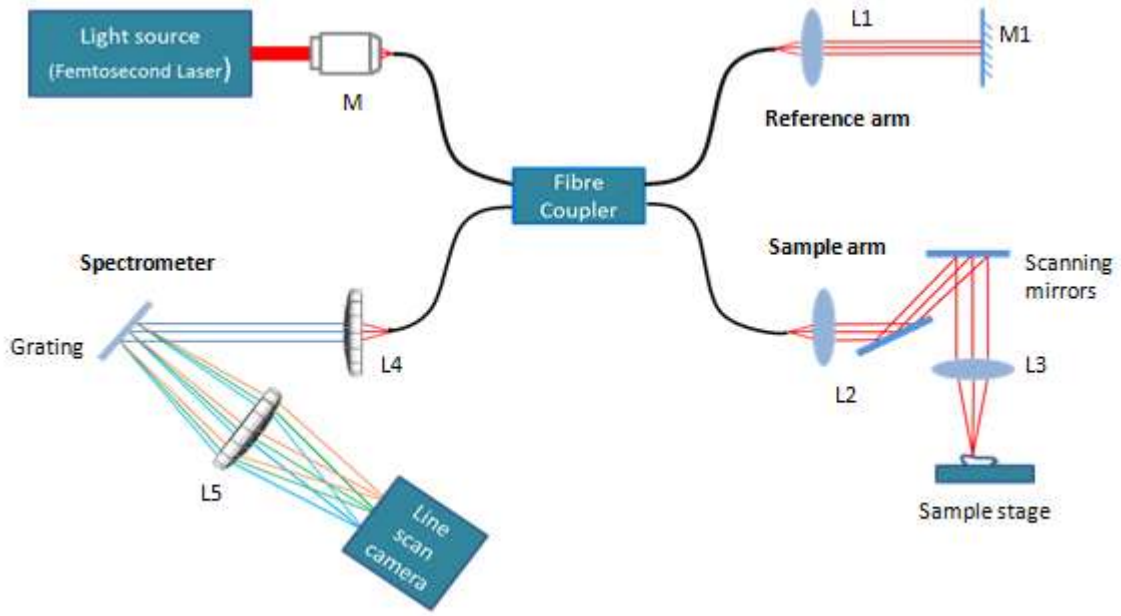

Figure 3.7: Schematic of the OCT set-up

The OCT setup made use of a femto-second light source (from Coherent Laser), which emitted light with a central wavelength of 800 nm and a spectral bandwidth of 260 nm. A 20x magnifying objective (M) is used to couple the laser light from the source onto an optical fibre. A fibre coupler is used to split the light into two arms, reference and sample arm. The reference arm consists of a collimating lens (L1; focal length 100 mm) and a retro reflector (M1) for reflecting all the light back into the reference arm. The sample arm consists of a collimating lens (L2) to provide a collimated beam of light onto the transverse scanning mirrors. Transverse scanning and image acquisition are all controlled and synchronized by voltage control waveforms, through Labview and DAQ boards. The beam is then focused onto the sample by means of lens L3 of focal length 30mm. The interference signal generated by the interference of light beams from the two arms is collected and measured by the use of a spectrometer. The spectrometer consists of a collimating lens L4 of focal length 75 mm, in order to ensure that a collimated beam falls on the grating. The dispersive element is a reflective ruled grating (from Thorlabs make) with a groove density of 1200 lines per mm. The grating is placed at an angle of approximately $\sim 30°$ to the incident light beam. A focusing lens of 55mm is used to focus the separated out wavelengths onto a line scan

camera (-Basler sprint-) with an array of 2048 pixels. The camera records the intensity distribution as a function of wavelength. This data is processed using a work station to yield OCT images.

Chapter 4

Data Processing

4.1 SD-OCT Data Processing

The image data obtained from the SD-OCT system, that is, the output of the spectrometer recorded on the CCD is referred to as 'Raw Data' and it consists of intensity values as a function of wavelength. Various signal processing methods are applied to the raw data for image reconstruction. Processing can be the bottleneck of the system when the objective is to obtain images of the tissue real time while scanning. There are several steps involved in image reconstruction which not only includes conversion of the raw data into z-domain, but also data processing steps to improve the quality of images obtained. Quality of OCT images can be improved by implementing methods of noise removal, improving resolution, reducing speckle, dispersion corrections and so on.

Data processing is the main deciding factor for the speed of the system and image quality. Hence it is a time consuming component of the SD-OCT system design and the methods should be carefully chosen and evaluated. This chapter details the data processing methods used to obtain reconstructed images from the system. In Spectral domain OCT, the data collected is the interference spectrum $I(\lambda)$, that is, spectral intensities as a function of wavelengths. The sample's axial reflectivity depth profile can be obtained by applying a Fourier transform over the corresponding modulated optical spectrum. But before applying the Fourier transform, the conversion from λ domain to k (or, wavenumber) domain is necessary. This is because the Fourier transform pair of z, the axial depth of the sample, is complementary to wavenumber, k. The steps involved in reconstruction of axial profile from an A scan is given in Figure 4.1.

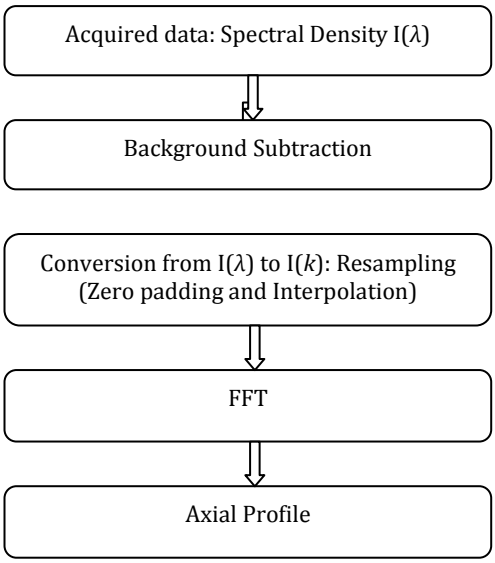

Figure 4.1: Algorithm followed for the reconstruction of axial profile from an A-scan

To suppress auto-correlation, self-cross correlation and camera artefacts, spectral interferograms at each slice along the x-direction were ensemble averaged at each wavelength to obtain reference spectrum. This background spectrum is then subtracted from each A-scan [7]. In order to use the FFT algorithm to compute the Fourier transform, the input to it must be uniformly sampled. If not, the resulting images would be characterized by a depth-dependent increase in axial resolution. The signal detected by the spectrometer is sampled almost uniformly in λ-space, but due to the nonlinear relationship between the wavelength (λ) and wavenumber (k), the data will not be evenly spaced in k-space. Therefore, to reconstruct images with high quality, spectral calibration is required, and the data has to be re-sampled in k-space in a way that is equally-spaced prior to applying the Fourier transform[3],[6].

Figure 4.2 shows the various steps involved in reconstruction where the plots correspond to reconstruction of raw data of finger skin.

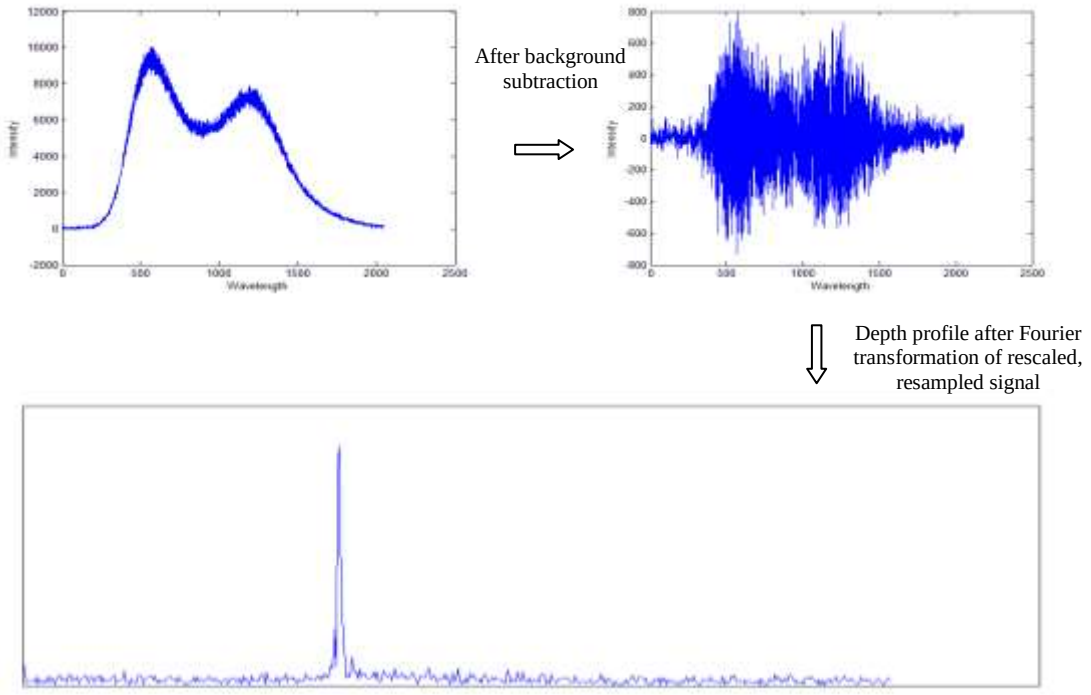

Figure 4.2: The various steps involved in reconstruction of image from raw data

4.2 Spectral Calibration and Resampling

It is necessary to map the relation between the pixel number and wavelength. This is termed as spectral calibration and it significantly affects the accuracy of the interpolation algorithm.

For spectral calibration, the general approach is to measure the interference spectra at two different positions [6],[8]. This eliminates the impact of dispersion mismatch and thus accurately assigns the wavelength to each pixel in the detector. First, the phase of the spectrum at the optical path difference (OPD) z_1 is extracted using the Hilbert transform. The same procedure is repeated for the optical path difference z_2. The difference between two phases ($\Delta\phi$) is calculated. The wavenumber k is obtained by $\Delta\phi / \Delta z$, $\Delta\phi = \phi_2 - \phi_1$ and $\Delta z = (z_2 - z_1)$. Doing so eliminates the impact of the dispersion mismatch. The vector of *N*, pixel number, as a function of k is fitted by a polynomial[6]. The corresponding curve may then be used for the interpolation and resampling step prior to the inverse Fourier transform. Cubic spline interpolation technique is most commonly used as it is more accurate compared to the nearest neighbour and linear interpolation methods.

In this thesis, the method given in [11] was followed to generate the calibration curve for resampling. Suppose N is the number of pixels on the CCD and $\lambda_{\min}$, $\lambda_{\max}$ defines the range of wavelengths captured by the spectrometer, then the N linearly spaced k values between the wavelength range is given by

$$k_i = \frac{2\pi}{\lambda_i} = 2\pi\left(\frac{1}{\lambda_{\max}} + \frac{i}{N-1}\left(\frac{1}{\lambda_{\min}} - \frac{1}{\lambda_{\max}}\right)\right) \text{ , } i = 0,1,2,..N-1 \tag{4.1}$$

λ_i corresponding to each of the linearly spaced sample k_i can be related by means of a non-linearity parameter S_i as shown below,

$$\lambda_i = \lambda_{\min} + S_i . \frac{\lambda_{\max} - \lambda_{\min}}{N-1} \text{ ,} \tag{4.2}$$

where S_i can be written as,

$$S_i = \frac{N-1}{\lambda_{\max} - \lambda_{\min}}\left(\left[\frac{1}{\lambda_{\max}} + \frac{i}{N-1}\left(\frac{1}{\lambda_{\min}} - \frac{1}{\lambda_{\max}}\right)\right]^{-1} - \lambda_{\min}\right) \tag{4.3}$$

The above equation is the calibration curve that provides the interpolation points for resampling the recorded interference spectrum to get a uniformly sampled spectrum in k space. The calibration curve used for resampling in this setup is shown in Fig. 4.2.

The next step in the signal processing chain is interpolation. Interpolation is a technique used to obtain new data points within the range of a discrete set of known points. Most commonly used interpolation algorithms are: nearest neighbour (0^{th} order), linear (1^{st} order) and cubic b-spline (3^{rd} order) interpolation. Linear interpolation is simple but yields less accurate results. Cubic B-spline interpolation gives satisfactorily accurate results but is computationally intensive. In cubic B-spline interpolation, a cubic polynomial describes data range between known points. This approach makes sure that the whole set of data is taken into account for the interpolation, unlike the linear method.

The accuracy of interpolation techniques can be greatly increased by upsampling the spectral data. This is carried out by a sequence of steps which are: performing FFT, zero padding the resulting spectrum, and then performing an IFFT. Upsampling by a factor of two was performed in this reconstruction.

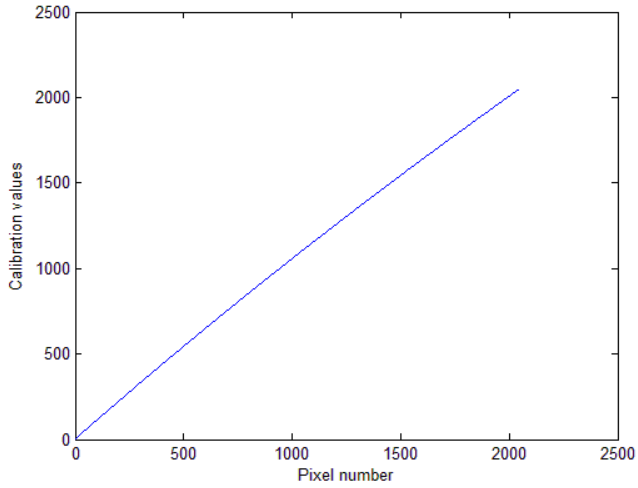

Figure 4.3: Set of calibration values used in this experimental setup to resample the spectrum

4.3 Results of data processing on raw data

The raw data for reconstruction was obtained from the commercial OCT machine Hyperion Spectral Domain OCT from Thor Labs. The machine uses an SLD light source with a central wavelength of 930 nm and a bandwidth of 100 nm. The axial resolution in air is about 5.8 µm. Reconstruction algorithms as described above, were applied on the raw data from the machine to obtain images of various tissues.

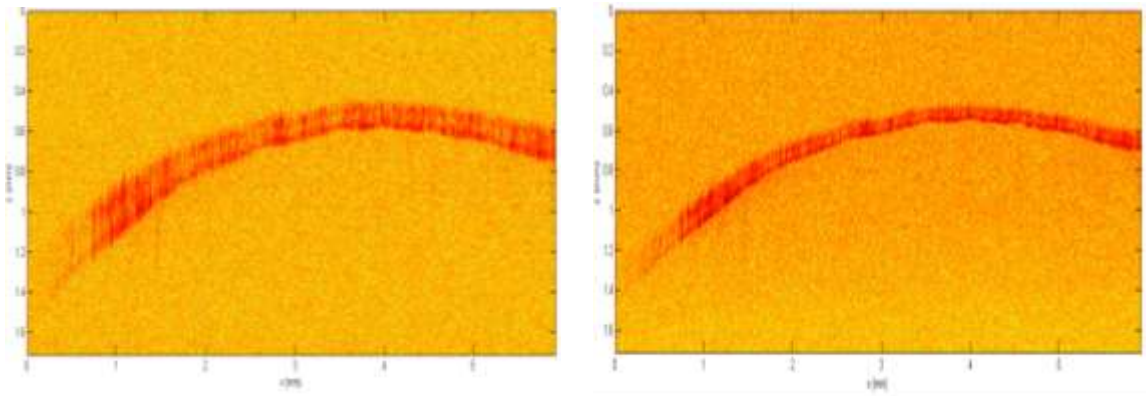

(a) **(b)**

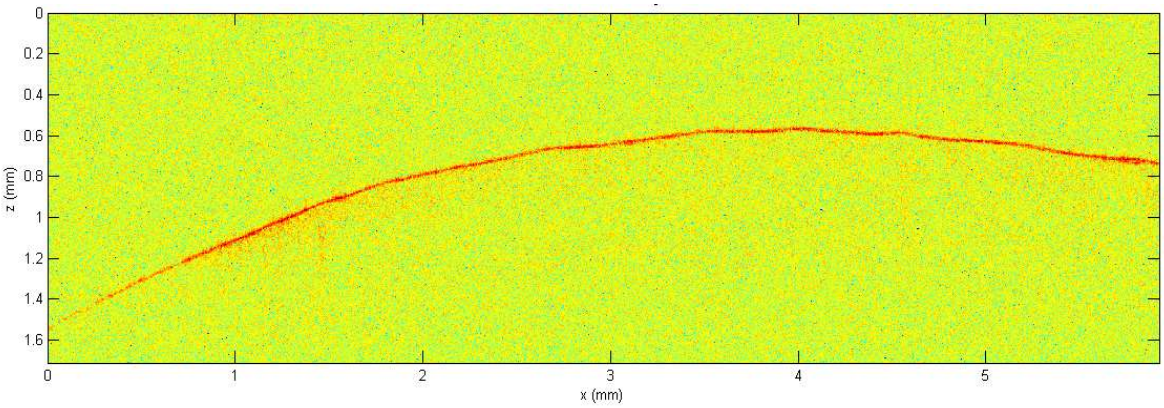

(c)

Figure 4.4: Reconstructed images from rawdata of fingernail (a) without resampling (b) with resampling but without zero padding before interpolation (c) with resampling and zero padding before interpolation, where the zero padding was done to upsample the signal by a factor of two

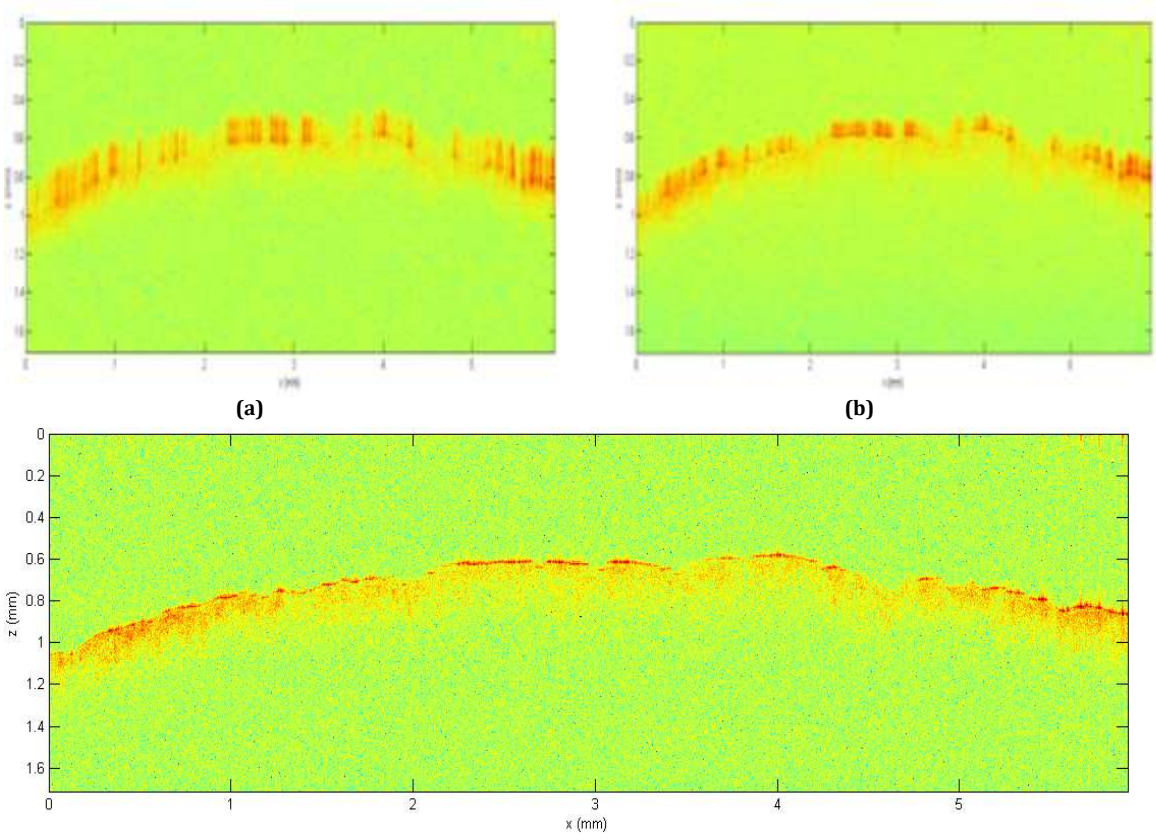

(a) **(b)**

(c)

Figure 4.5: Reconstructed images from raw data of finger tissue (a) without resampling (b) with resampling but without zero padding before interpolation (c) with resampling and zero padding before interpolation, where the zero padding was carried out to upsample the signal by a factor of two

The images obtained by performing reconstruction on raw data were compared with reconstructed images from the Thorlabs OCT machine. The comparison is shown in Fig. 4.6.

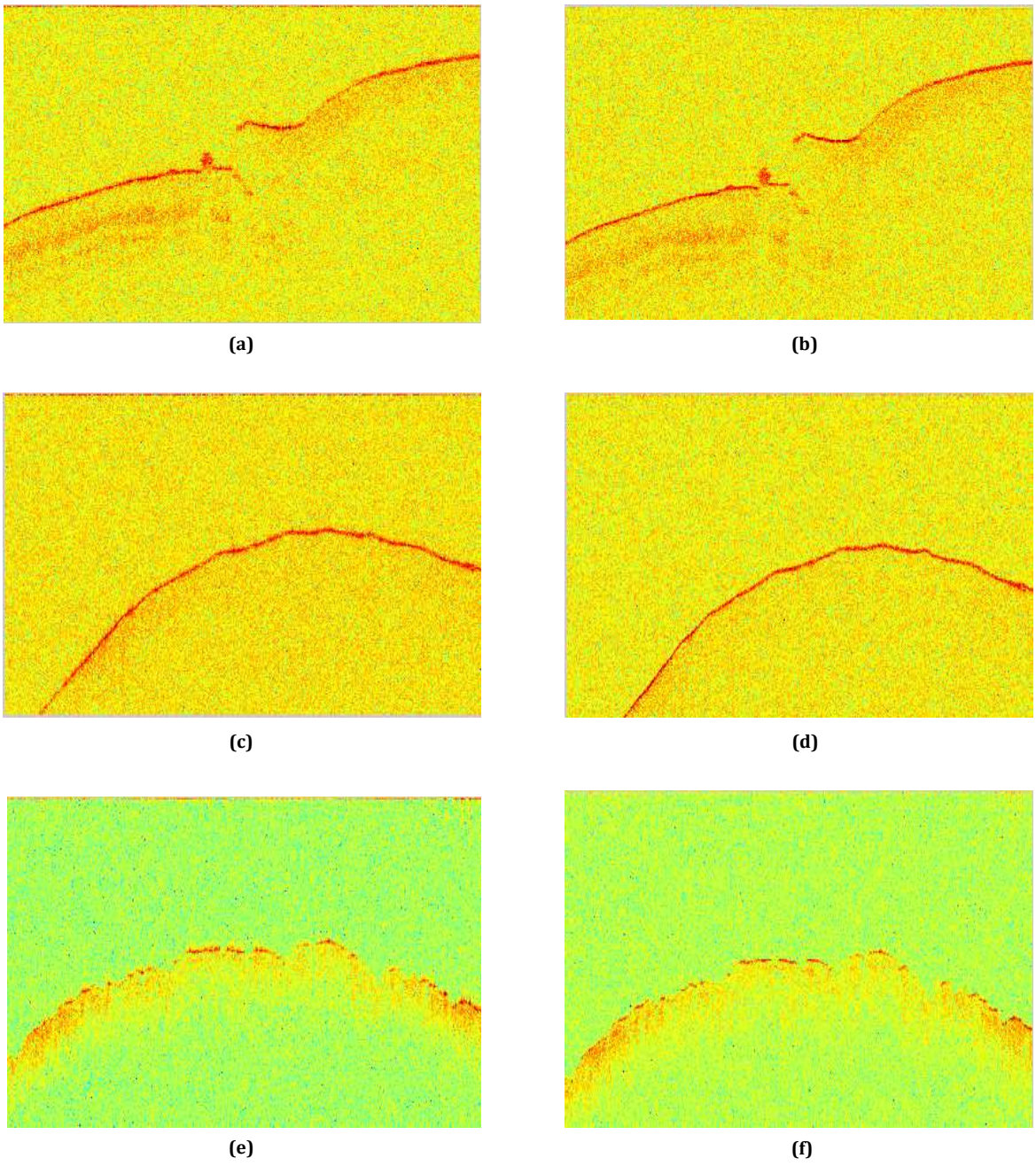

(a) **(b)** **(c)** **(d)** **(e)** **(f)**

Figure 4.6: Comparison of reconstructed images: (a), (c) and (e)- Images reconstructed using the in-house algorithm; (b), (d) and (f)- Images from the standard OCT machine

For the purpose of 3D visualization, the images were converted to grayscale and then loaded in software Amira. The reconstructed images in grayscale displayed a considerable amount of noise. For noise removal, they were subjected to thresholding and median filtering. The filtered grayscale images were used as 3D datasets for viewing. The following figures show the results of reconstruction of 3D raw OCT data and the corresponding volumetric visualization.

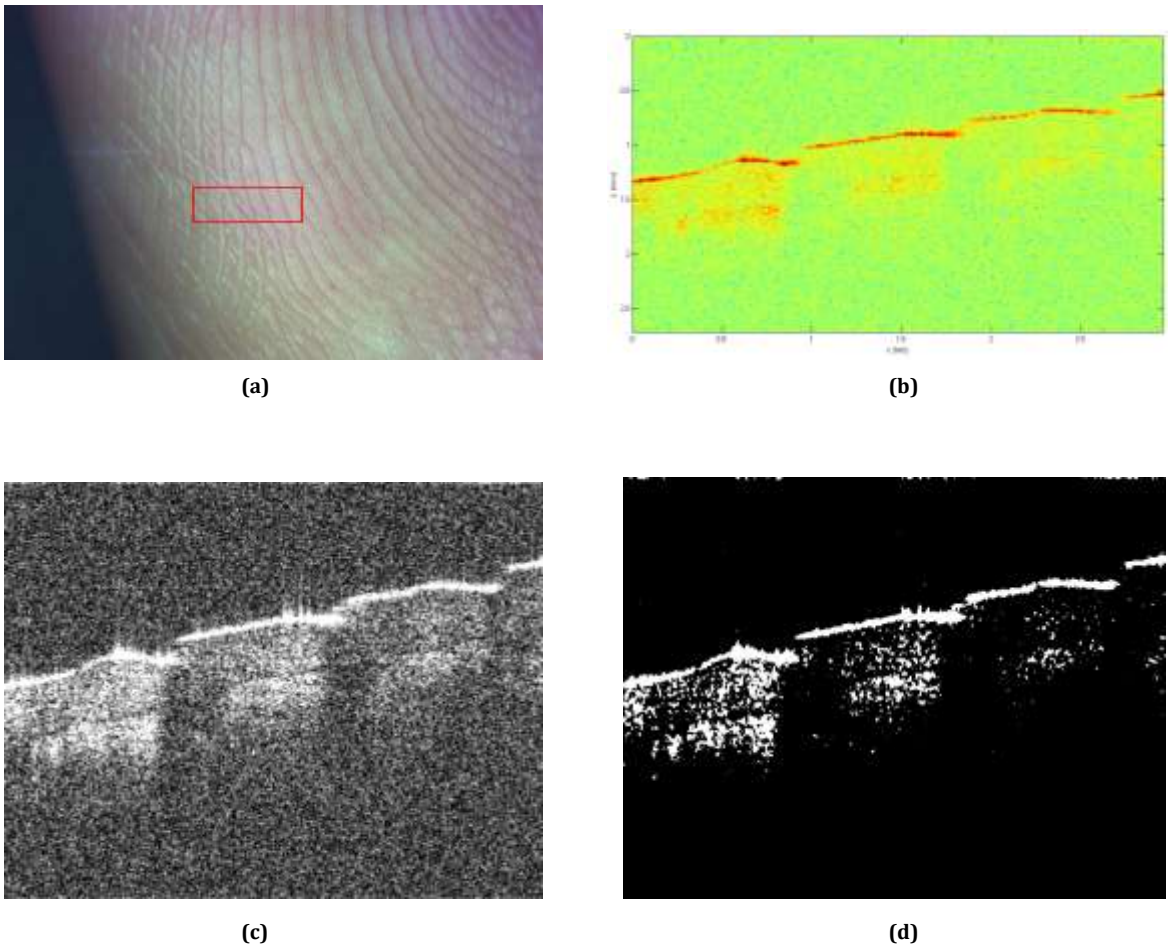

(a) **(b)**

(c) **(d)**

Figure 4.7: (a) Volume scan of finger tissue (b) A reconstructed 2D slice in RGB format (c) Corresponding grayscale image (d) Image after proper filtering

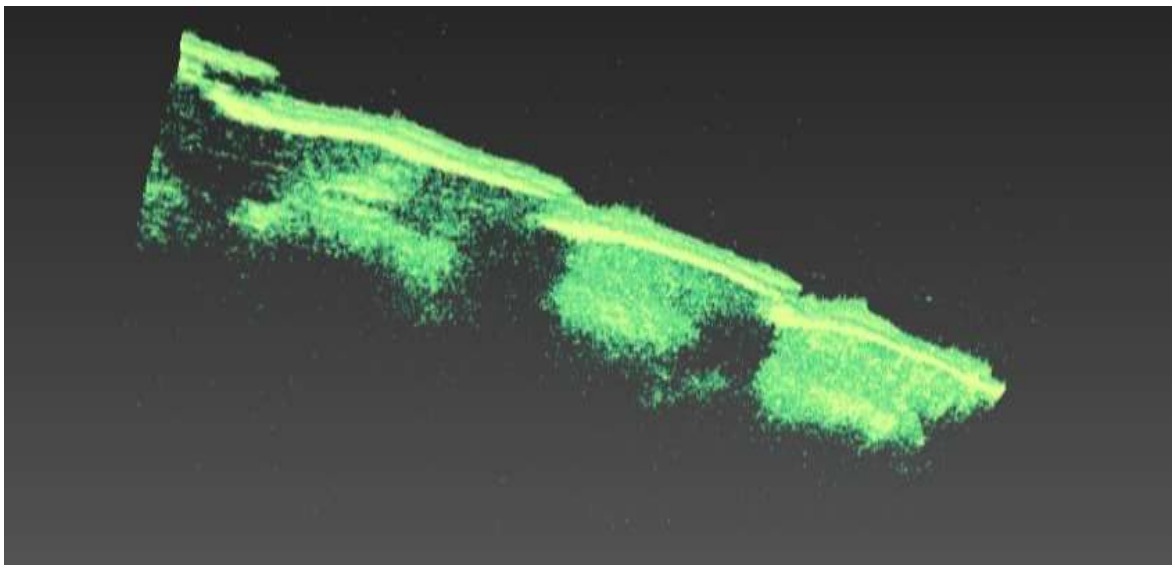

Figure 4.8: Volumetric view of a section of the 3D data-set

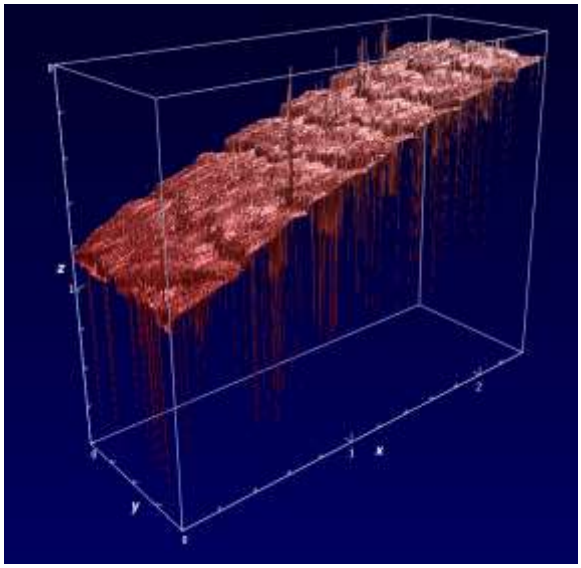

(a)

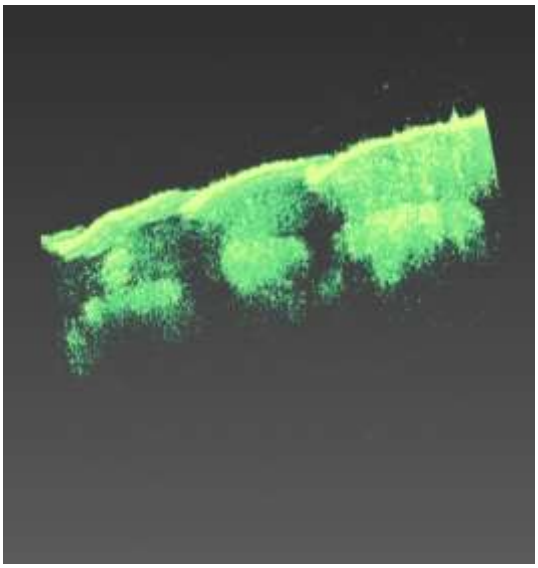

(b)

Figure 4.9: A comparison of the volumetric reconstruction with that of the Thorlabs reconstruction (a) 3D image from the Thorlabs machine (b) 3D image obtained by our reconstruction (Note: Only a small section of the data-set reconstruction is shown)

Chapter 5

Nanosensitive OCT

5.1 Introduction to ns-OCT

OCT is a rapidly growing technology finding its applications in various fields, particularly, biomedical imaging. Many recent advancements in this technology has brought about tremendous improvements in resolution, imaging range etc. However, it suffers from the drawback that the resolution and sensitivity to structural changes is limited to less than 10 μm[32] and in the best ultra-high resolution OCT techniques, it can reach upto 1μm. Many biological processes in living tissue involve structural changes at the nanoscale, hence, if OCT can provide increased resolution and sensitivity to nanoscale alterations, it would open a new plethora of applications for OCT.

The major area of interest in this regard, is cancer, where the pathogenesis leads to structural changes in the cell nucleus, attributed mainly to changes in the 3D spatial arrangement of chromatin patterns or DNA material within the nucleus, during the process of carcinogenesis[33]. Therefore, the identification of nanoscale structural changes, prior to the presence of microscale morphological changes, can be used to diagnose the disease at its early stages. This would be a significant achievement in the early diagnosis and prognosis of cancer. Nanoscopy can achieve such detection at nanoscales, but it suffers from drawbacks such as the requirement of labelling (largely required), cost and inability to image *in vivo*.

Various approaches have been investigated to increase the imaging capability of optical imaging techniques to study micron-sized structures beyond the diffraction limit of optical system resolution[34, 35]. For depth-resolved measurements of 3-D profile of cell nuclei, light scattering

spectroscopy (LSS) has been incorporated in OCT [36]. Molecular imaging was made possible by exploiting spectral information from the OCT data[37]. ISAM (Interferometric Synthetic Aperture Microscopy) employed computed imaging techniques in OCT data to reconstruct out of focus areas, thus making it possible to resolve features outside of the confocal region[38]. Recently, phase-sensitive OCT has been applied for the measurement of vibrations in the hearing organs[39] and studies of the human retina[40] and cornea with nanoscale sensitivity. Several studies have suggested the possibility that OCT can be made sensitive enough to detect nano-structural changes in biological tissue samples[41].

Spectral Encoding of Spatial Frequency (SESF) is a novel approach to characterize the nanometer scale axial structural alterations in objects[42]. It is based on an analysis of the Fourier space of scattered light. Nano-sensitive OCT is based on the SESF approach to detect nanoscale structural changes in tissues. It has been demonstrated that label-free sensing of depth resolved nano-structural changes is possible by the use of this technique[43]. Structural information about a 3D object, spectrally encoded in the remitted light, are transformed from the Fourier domain into each voxel of the 3D OCT image without compromising sensitivity[43]. In this thesis, nano-sensitive OCT based on SESF approach was used to investigate its ability to perform nanomorphology characterization.

5.2 Principle of ns-OCT

This technique is based on the concept that the structure of a scattering object can be described using a 3D function called the scattering potential,

$$F(r) = \frac{1}{4\pi} k^{2} \left[n^{2}(\mathbf{r}) - 1 \right] \tag{5.1}$$

where, $\mathbf{K}$ is the scattering vector, n is the free-space refractive index, $\mathbf{r}$ is the location within the object and k is the wave number.

For large values of $\mathbf{r}$,

$$\mathbf{K} = \frac{2\pi}{\lambda}(\mathbf{s} - \mathbf{s_0}) = \mathbf{k_s} - \mathbf{k_i} \tag{5.2}$$

where, $\mathbf{s}$ is the unit vector of scattered wave and $\mathbf{s_0}$ is the unit vector of illumination wave.

If the illuminating plane-wave is incident at angle θ, the scattering amplitude in the far field, according to the Born approximation is given by,

$$f_s(\mathbf{k_i},\mathbf{k_s}) = \int_{V(\mathbf{r}')} F(\mathbf{r}')\, e^{i(\mathbf{k_s}-\mathbf{k_i}).\mathbf{r}'}\, d^3\mathbf{r}' \tag{5.3}$$

The Fourier transform of scattering potential is,

$$\tilde{F}(\mathbf{K}) = \int F(r)\, e^{-i\mathbf{K}.\mathbf{r}}\, d^3 r \tag{5.4}$$

Hence, the Eq. (5.3) becomes,

$$f_s(\mathbf{k_i},\mathbf{k_s}) = \tilde{F}(\mathbf{K}) = \tilde{F}\left(k(\mathbf{s}-\mathbf{s_0})\right) \tag{5.5}$$

According to the first Born approximation, when an object is illuminated by a monochromatic plane wave, the complex amplitude of the scattered wave at a given wavelength in the far zone, for a given direction, depends entirely on only one Fourier component of the 3D scattering potential, given by the vector $\mathbf{K}$ [44]. The Fourier components of scattering potential in $\mathbf{K}$ space is represented as an Ewald's sphere as shown in Figure 5.1(b). Since the numerical aperture (NA) of the light collecting components are limited, the accessible spatial frequencies are restricted, which can then be represented as an Ewald's sphere cap. Instead of monochromatic light, if a range of wavelengths is used for illumination, there will be an Ewald's sphere cap corresponding to each wavelength, resulting in a muffin shaped region of spatial frequency support as shown in Figure 5.1(c) (for reflection geometry). Every point on the Ewald's sphere corresponds to a 3D spatial frequency vector $\mathbf{K}$ which can be expressed in the following form in Cartesian coordinates

$$\mathbf{K} = k_x\mathbf{x} + k_y\mathbf{y} + k_z\mathbf{z} = 2\pi\left(\nu_x\mathbf{i} + \nu_y\mathbf{j} + \nu_z\mathbf{k}\right) \tag{5.6}$$

where, ν_x, ν_y, ν_z are the spatial frequencies in Cartesian coordinates given by,

$$\nu_x = n\left(\sin\alpha - \sin\theta\right)\cos\phi \,/\, \lambda, \tag{5.7}$$

$$\nu_y = n\left(\sin\alpha - \sin\theta\right)\sin\phi \,/\, \lambda \tag{5.8}$$

$$\nu_z = n\left(\cos\theta + \cos\alpha\right) / \lambda \tag{5.9}$$

where, θ is the illumination angle, α is the scattering angle, ϕ is the azimuthal angle and n is the refractive index.

We can obtain the Fourier transform of the 3D scattering potential if we can measure the scattered field for all possible wavelengths and at all angles of illumination and scattering. Once we have the data in Fourier space, then we can perform a 3D inverse Fourier transform to get the scattering potential.

$$F(\mathbf{r}) = \frac{1}{(2\pi)^3}\int \tilde{F}(\mathbf{K})\, e^{-iK.r}\, d^3K \tag{5.10}$$

The limitation is that there a restriction on the range of spatial frequencies, therefore, the reconstructed scattering potential will be a low pass filtered approximation, and the maximum achievable resolution is about λ/2.

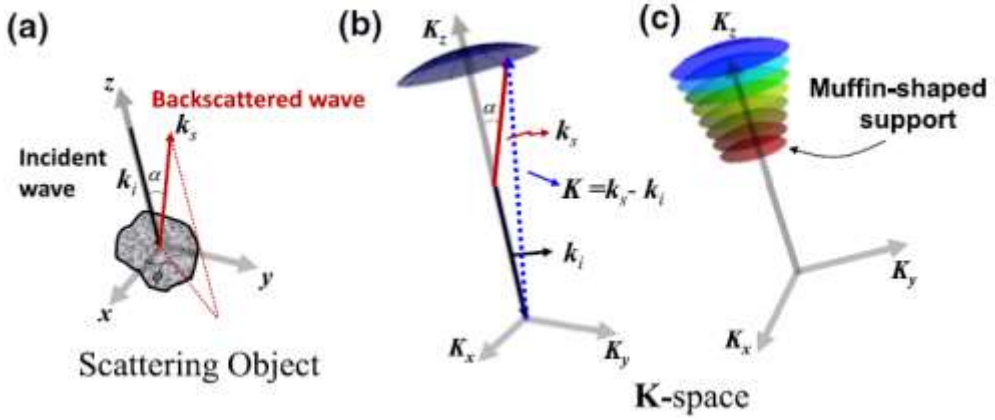

Figure 5.1: Illustration of the scattering vectors in K-space for reflection configuration. (a) Interaction of light interaction with a scattering object (b) Scattering vector in K-space for a single wavelength (c) Representation of scattering vectors in K-space for multiple wavelengths

For a moderate value of α, axial spatial frequency and wavelength have a one-to-one correspondence (from Figure 5.2 and Eq. (5.9)). This is the underlying principle behind the SESF approach. The idea is that axial spatial frequencies can be encoded in terms of wavelength, translated from the Fourier to image domain and mapped to each voxel of the 2D image.

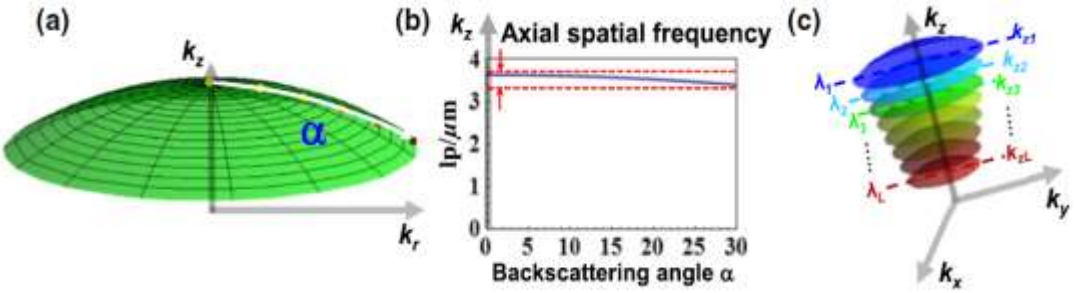

Figure 5.2: The correspondence between wavelength and axial spatial frequency in the reflection configuration. (a) Representation of Ewald's sphere cap at a normal incidence in the reflection configuration. (b) Showing the weak dependence of axial spatial frequency k_z on the backscattering angle or lateral spatial frequency k_r (c) Encoding each wavelength by an axial spatial frequency k_z with a small uncertainty which is shown in (b)

In OCT, we obtain the Fourier components in the axial direction only. Image reconstruction in FD-OCT is based on the inverse scattering principle discussed above, the difference being that, in Fourier domain OCT, it's a one-dimensional problem. Hence a simplified form of the Eq. (5.10) , i.e., a 1-D inverse Fourier transform can be used to reconstruct the axial components of the 3D scattering potential. The resolution of OCT system depends on the spectral bandwidth. In order to improve resolution, one can increase the spectral range, but in nanosensitive OCT, a different approach is used to increase the resolution and sensitivity of OCT to detect nanoscale structural changes.

From the earlier discussion, we can derive the following,

$$\nu_z = \frac{2n}{\lambda} \quad , \quad H_z = \frac{1}{\nu_z} \tag{5.11}$$

Ns-OCT is able to characterize the internal structure of an object with nanoscale accuracy, which describes the precision to quantify the structural characteristics and it does not mean nanoscale resolution.

To realize ns-OCT, the first step is to convert the spectral intensity data I(λ) to intensities as a function of axial spatial frequencies I(υ), using the relation in Eq. (5.11). The complex spectrum of axial spatial frequencies is then divided into a number of sub-bands. This step actually performs decomposition of the muffin-shaped $\mathbf{K}$-space support into slices along the z-axis[45]. Suppose we divide the source spectrum into L spectral sub-bands, and each sub-band can be labelled by its mean wavelength λ_l, where $l = 0,1,2,...L-1$. We can label the volume of each $\mathbf{K}$-space slice corresponding to the l^{th} spatial frequency sub-band by the spatial period H_{zl}. The number of sub-bands chosen determines the number of points of reconstruction for the axial spatial periods.

The object space is also divided into several volumes of interest (VOI), indexed by $m = 0,1,2,...M-1$. The width of each sub-band decides the axial extent of the VOI within the object. If υ_{zl} is the spatial frequency range each of the l sub-bands, then the minimum axial size of the voxel is given by,

$$\Delta z = \frac{1}{2\Delta\nu_{zl}} \tag{5.12}$$

The smallest lateral extent of the VOIs is decided by the diffraction limited lateral resolution of the reconstructed object.

Next, we compute the energy contribution of the E_m of the l^{th} spectral sub-band to the spatial period profile of the m^{th} VOI at H_{zl} as,

$$E_m(H_{zl}) = \int_{V_m} \left| F_{m,l}(\mathbf{r}) \right|^2 d\mathbf{r}\,, \tag{5.13}$$

where, V_m is the integration volume of the m^{th} VOI and $F_{m,l}(\mathbf{r})$ is given by the inverse Fourier relation,

$$F_{m,l}(\mathbf{r}) = \frac{1}{(2\pi)^3} \int_{K_l} F(\mathbf{K})\, e^{-i2\pi K.r_m}\, d\ \mathbf{K} \tag{5.14}$$

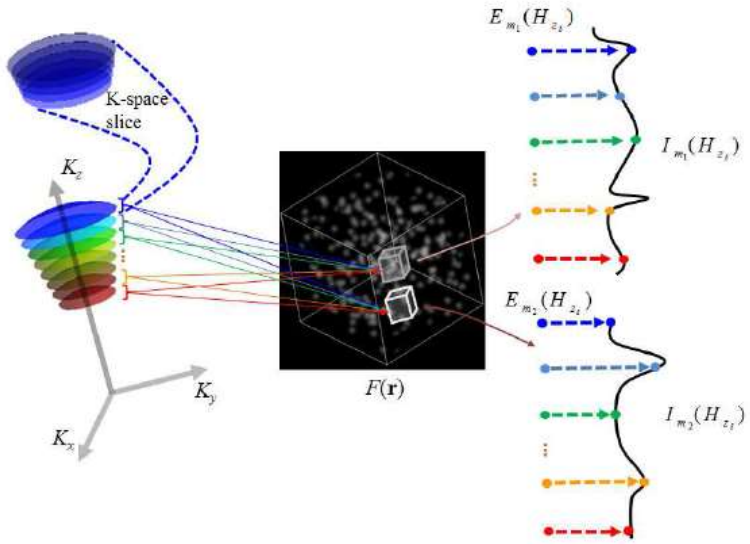

Figure 5.3: Illustrating how the K-space is divided into sub-bands and structural characterization via mapping of energy contributions of the various sub-bands

By calculating the energy contributions for all spatial periods H_{zl}, we can get the axial spatial period profiles for the m^{th} VOI. Repeating the same for all VOIs, we obtain the spatial period profiles for each voxel of the 3D image. For each voxel, the dominant axial spatial period is found out and then the ns-OCT image is formed as a colour map of the dominant spatial periods, which are nothing but the dominant axial structure sizes.

5.3 Data Processing for ns-OCT

The OCT data for processing was obtained from the Hyperion SD-OCT system (Thor Labs). It uses a broadband SLD light source with a central wave length of 930 nm and a bandwidth of 100 nm. The flow chart below shows the data processing steps required to obtain the ns-OCT images.

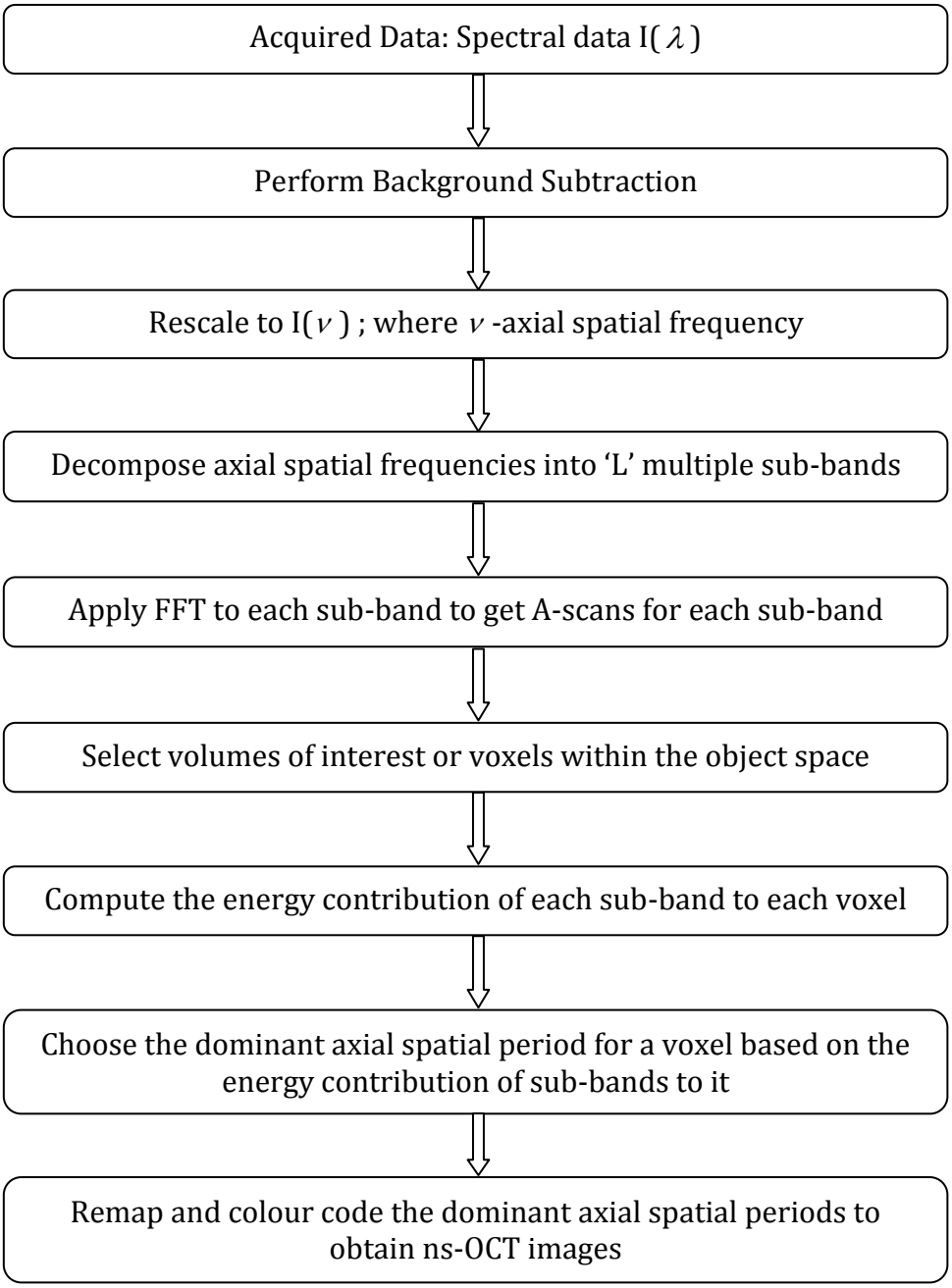

5.4 Results

Nanosensitive algorithm was applied on raw OCT data of finger nail and the eye of moth.For the procedure, the spectral range of 880 nm to 980 nm was divided into 16 sub-bands.The voxels chosen in the object space had the following size: axial extent ~26 μm, ~15 μm in lateral (x)

direction and ~16 µm. The axial extent of the voxel is chosen based on the number of sub-bands (according to Eq. (5.12)) and the lateral extents based on the lateral resolution of the system. The average axial spatial periods of the different sub-bands are given below in table 5.1.

Table 5.1: The average spatial periods Hzl, corresponding to 16 sub-bands

Sub-band	Hzl (nm)	Sub-band	Hzl (nm)
1	294.26	9	310.14
2	296.16	10	312.25
3	298.08	11	314.38
4	300.02	12	316.55
5	301.99	13	318.74
6	303.99	14	320.97
7	306.01	15	323.23
8	308.06	16	325.52

The first sample was obtained by *in vivo* imaging of finger nail. The following figures show the results of processing the raw OCT data.

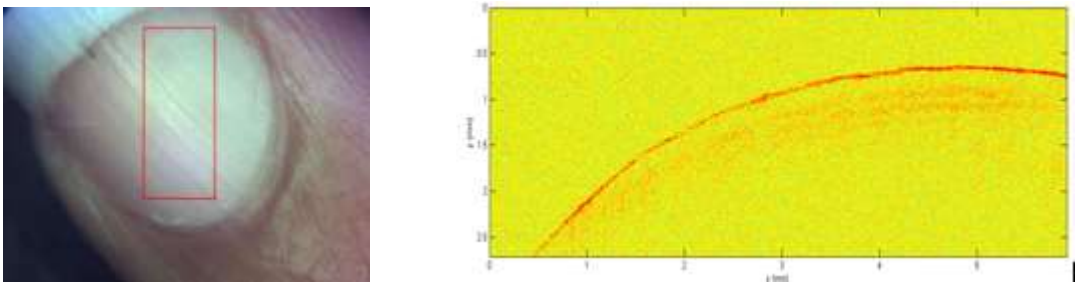

(a) **(b)**

Figure 5.4: (a) The region of volume scan is shown inside the red box (b) Reconstructed 2D image in RGB. It is one of the cross sections of the volume data

Figure 5.5: (a) shows the reconstructed grayscale image of a 2D slice. The image after appropriate filtering is shown in Figure 5.5: (b).

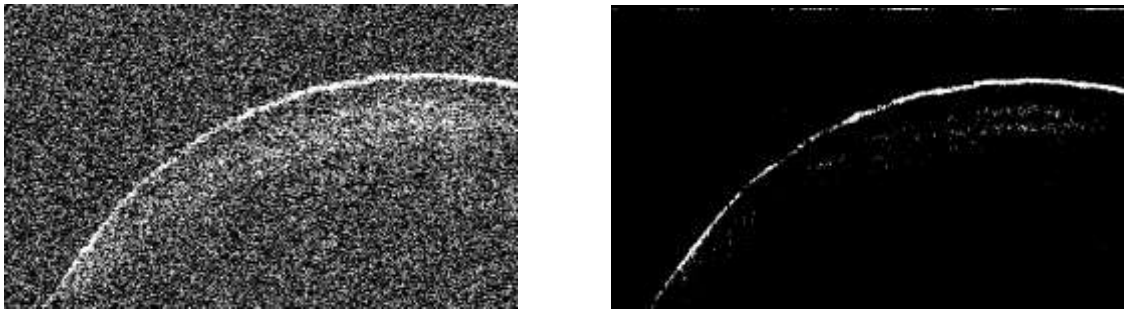

(a) **(b)**

Figure 5.5: (a) Grayscale image showing significant amount of noise (b) Image after noise removal through filtering

The reconstructed data after filtering was used to obtain 3D volumetric visualization. Volume rendering of the 3D data was performed by means of the software Amira. The corresponding images are shown in figures 5.6 and 5.7.

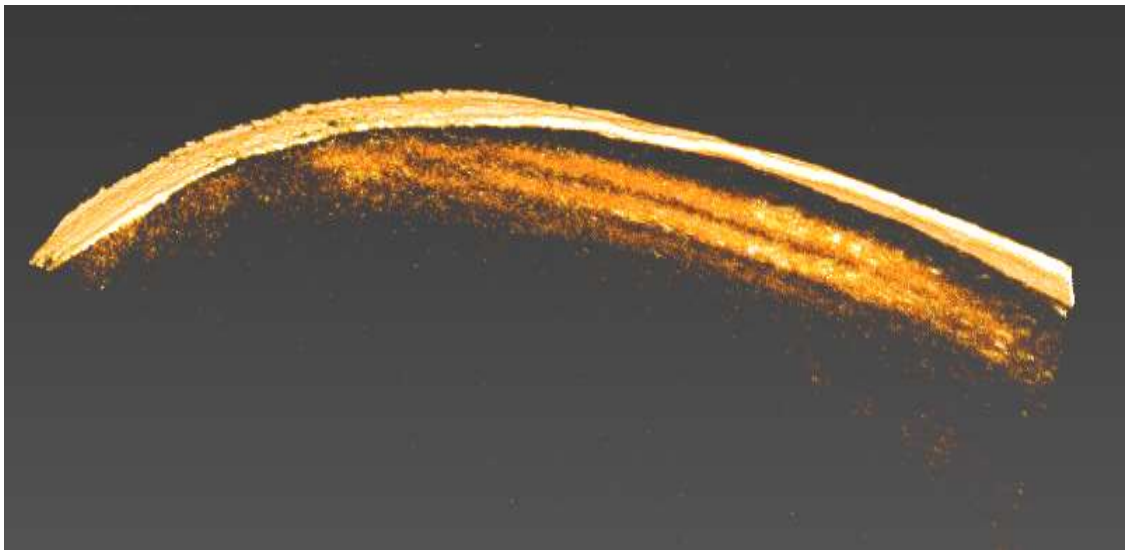

Figure 5.6: Volume rendered OCT image

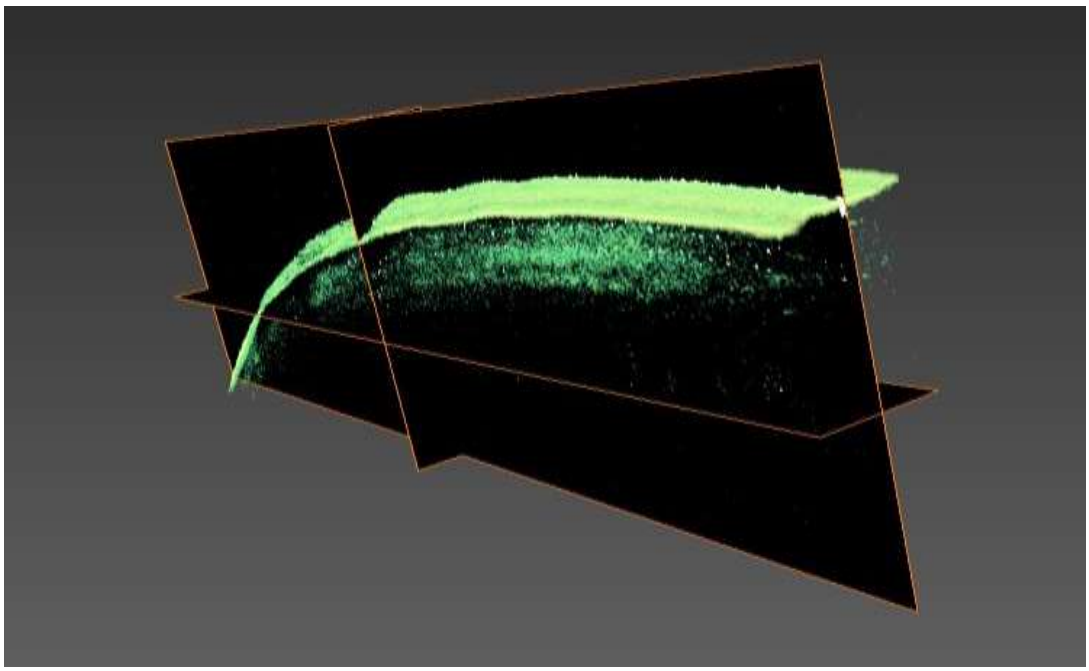

Figure 5.7: 3D image with sectional view

As seen from the above figures, structural size differences are not observable from conventional OCT images. Hence, ns-OCT technique was applied to the 3D OCT data. The following figures illustrate the use of this technique.

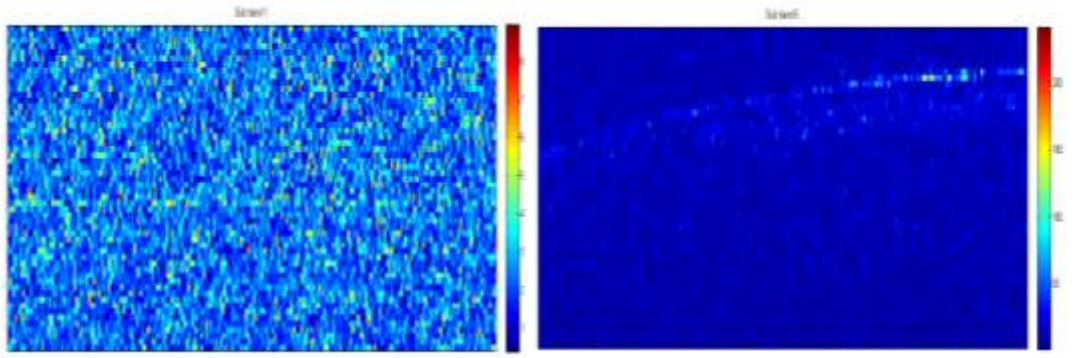

(a) **(b)**

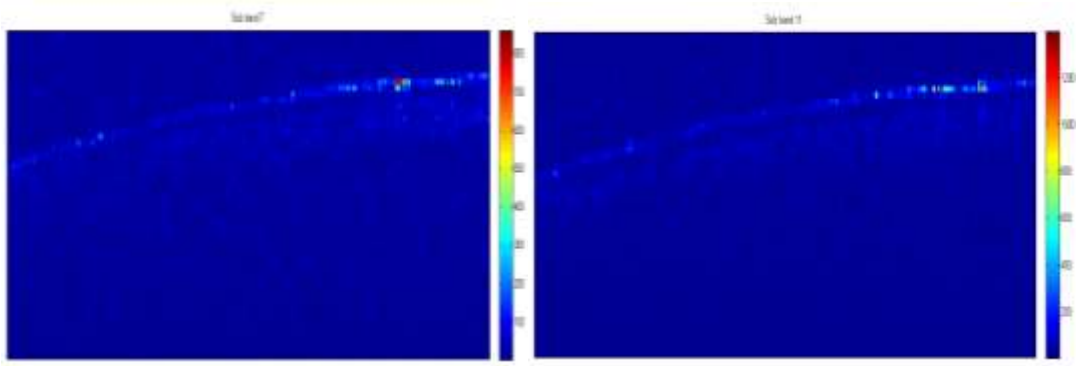

(c) **(d)**

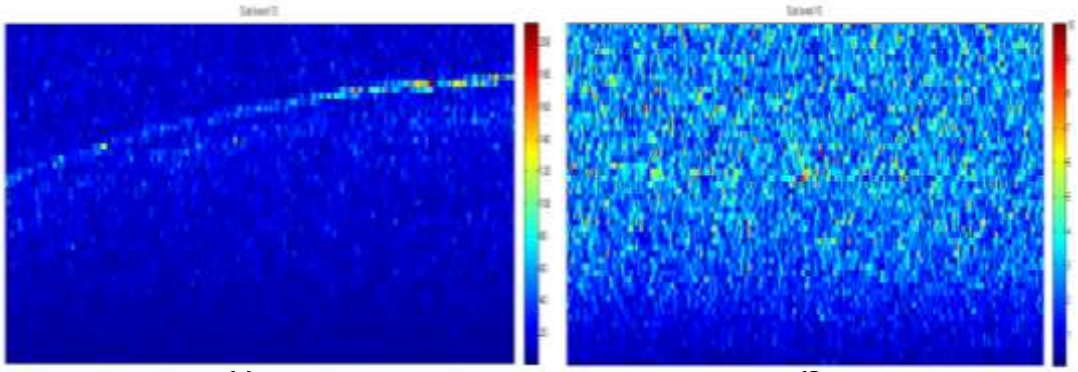

(e) (f)

Figure 5.8: (a)-(f) Energy contributions of different sub-bands; (a) sub-band 1 (b) sub-band 5 (c) sub-band 7 (d) sub-band 11 (e) sub-band 13 (f) sub-band 15

Figure 5.8 illustrates the energy contributions of few of the spectral sub-bands. The figure below shows the ns-OCT image, which is formed as a map of the dominant axial spatial periods. This figure enables the differentiation of axial structures on the basis of size, as dominant spatial period corresponds to the dominant size of the axial structures.

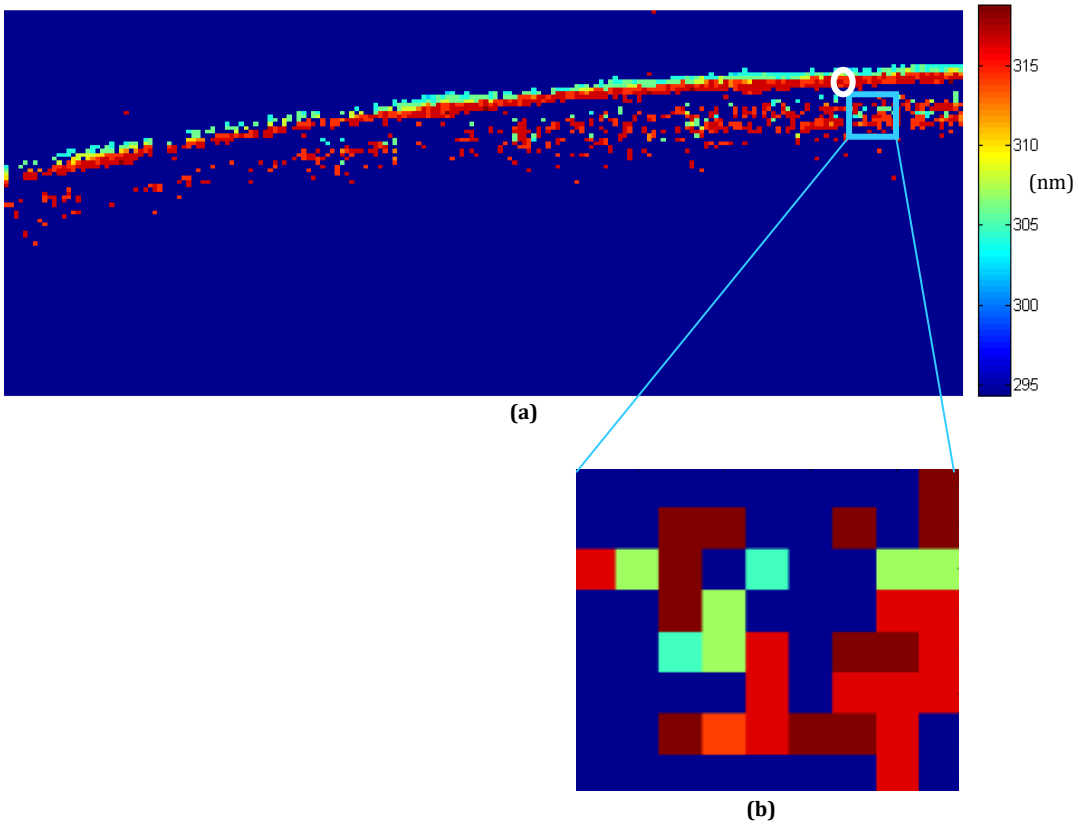

(a)

(b)

Figure 5.9: (a) Nanosensitive OCT image; formed as a map of dominant spatial periods (b) Magnified portion of ns-OCT image

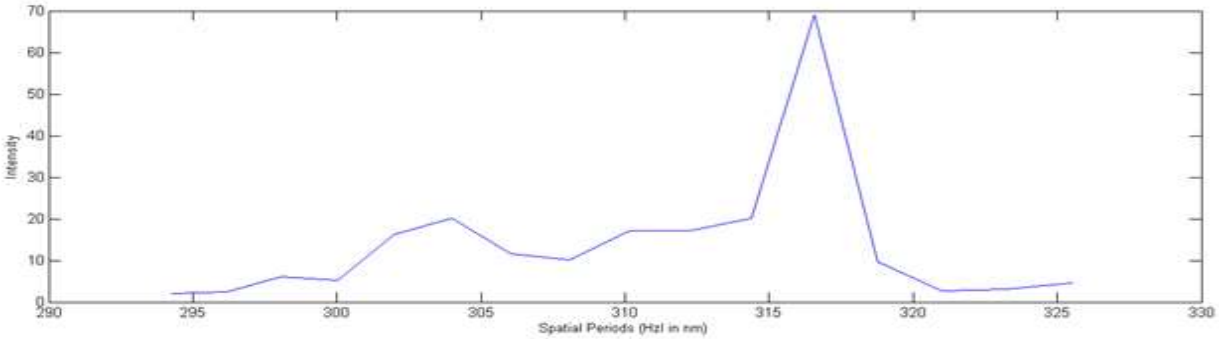

Figure 5.10: The profile of axial spatial period for a selected point in the ns-OCT image (point marked by white circle in Figure 5.9: (a) Nanosensitive OCT image; formed as a map of dominant spatial periods (b) Magnified portion of ns-OCT image)

The next sample was that of the eye of a moth. A moth's eye has a special anti-reflecting coating, which is a natural nanostructured film that eliminates reflections. This film has nano-sized structures consisting of bumps in a hexagonal pattern with their centres roughly 300 nm apart. This is why we chose the moth's eye as a sample for investigating the ability of ns-OCT to detect nanoscale changes. The ns-OCT image shows clearly the difference in the sizes of the structures in the nanometer scale.

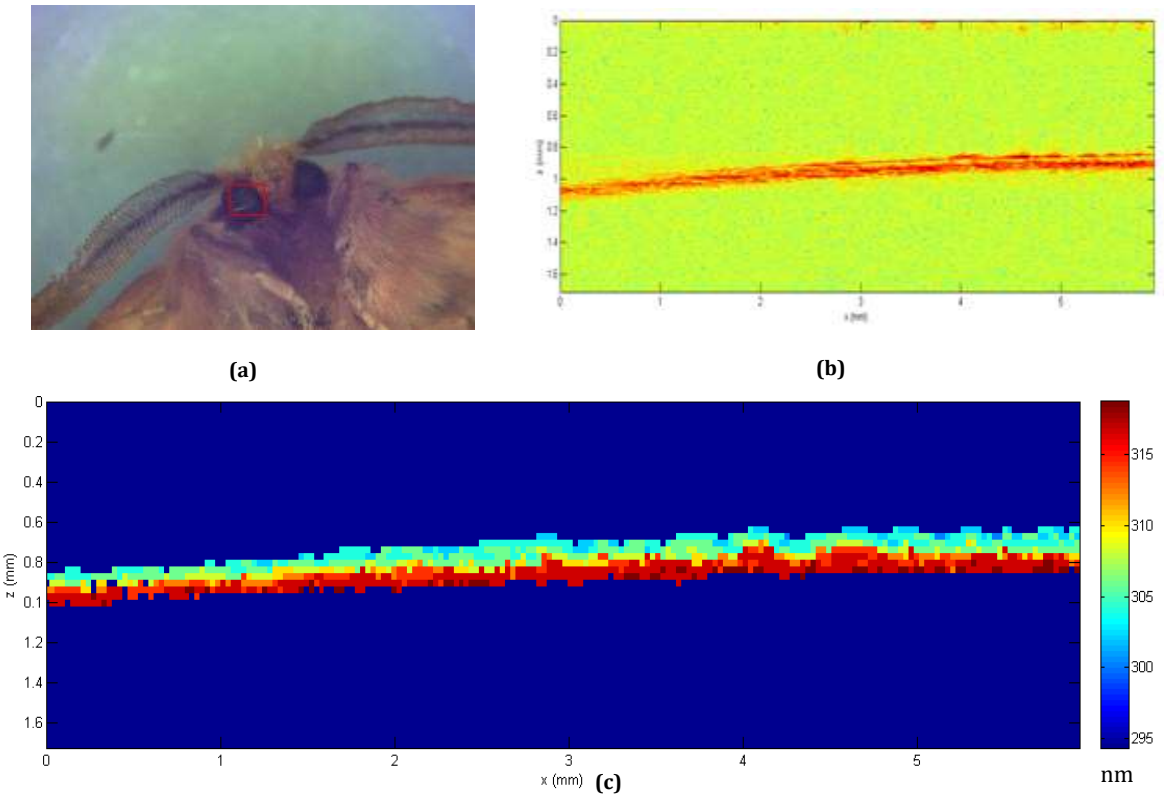

Figure 5.11 : (a) Image showing the region of volume scan of the compound eye of moth (b) Conventional OCT image (c) Nanosensitive OCT image; formed as a map of dominant spatial periods

.

Chapter 6

Summary and future work

Optical Coherence Tomography is a non-contact, non-invasive imaging modality that can image structures with micrometer resolution. Its finds particular applications in the imaging of biological tissues, as it can provide images of tissue samples with resolutions approaching that of histology. This makes it a potential diagnostic tool for detection of various diseases, especially cancer.

In this thesis, a Spectral-domain OCT set up was used to capture images of various tissues. The raw data from the OCT system was reconstructed with good image quality using efficient image reconstruction algorithms. Nano-sensitive OCT technique was further employed to improve the sensitivity of OCT to nanoscale, so that the nanometer sized structural alterations in a sample can be detected. The technique was demonstrated on a moth eye and finger nail to visualize the dominant spatial periods, and thereby, the dominant axial structures in the sample.

Future work can be aimed at applying the nanosensitive OCT technique to detect nanomorphology changes in the cells of tissues, which are associated with carcinogenesis. These nanoscale changes in cell nucleus are indicators of cancer, and such a possibility has a lot of potential in the identification of cancer at its early stages and prognosis. Efforts should be made in this direction to improve the resolution and sensitivity of OCT, so that it can be successfully applied as a convenient diagnostic tool

References

[1] Bellis, M., History of Microscopes. 2012.

[2] Huang, D., et al., Optical coherence tomography. Science, 1991. **254**(5035): p. 1178-1181.

[3] Fujimoto, J.G., et al., Optical biopsy and imaging using optical coherence tomography. Nature medicine, 1995. **1**(9): p. 970-972.

[4] Brezinski, M.E., et al., Optical coherence tomography for optical biopsy properties and demonstration of vascular pathology. Circulation, 1996. **93**(6): p. 1206-1213.

[5] Drexler, W. and J. Fujimoto, Optical Coherence Tomography: Technology and Applications, Biological and Medical Physics. Biomedical Engineering, 2008: p. 1346.

[6] Izatt, J., et al., Optical coherence tomography and microscopy in gastrointestinal tissues. Selected Topics in Quantum Electronics, IEEE Journal of, 1996. **2**(4): p. 1017-1028.

[7] Tearney, G., et al., Optical biopsy in human gastrointestinal tissue using optical coherence tomography. The American journal of gastroenterology, 1997. **92**(10): p. 1800-1804.

[8] Tearney, G., et al., Optical biopsy in human urologic tissue using optical coherence tomography. The Journal of urology, 1997. **157**(5): p. 1915-1919.

[9] Pitris, C., et al., High resolution imaging of the upper respiratory tract with optical coherence tomography: a feasibility study. American journal of respiratory and critical care medicine, 1998. **157**(5): p. 1640-1644.

[10] Tearney, G.J., et al., In vivo endoscopic optical biopsy with optical coherence tomography. Science, 1997. **276**(5321): p. 2037-2039.

[11] Jesser, C., et al., High resolution imaging of transitional cell carcinoma with optical coherence tomography: feasibility for the evaluation of bladder pathology. The British journal of radiology, 1999. **72**(864): p. 1170-1176.

[12] Sergeev, A., et al., In vivo endoscopic OCT imaging of precancer and cancer states of human mucosa. Optics express, 1997. **1**(13): p. 432-440.

[13] Feldchtein, F., et al., Endoscopic applications of optical coherence tomography. Optics express, 1998. **3**(6): p. 257-270.

[14] Brezinski, M.E., et al., Optical biopsy with optical coherence tomography: feasibility for surgical diagnostics. Journal of Surgical Research, 1997. **71**(1): p. 32-40.

[15] Boppart, S.A., et al., Optical coherence tomography for neurosurgical imaging of human intracortical melanoma. Neurosurgery, 1998. **43**(4): p. 834-841.

[16] Boppart, S.A., et al., Intraoperative assessment of microsurgery with three-dimensional optical coherence tomography. Radiology, 1998. **208**(1): p. 81-86.

[17] Pitris, C., et al., High-resolution imaging of gynecologic neoplasms using optical coherence tomography. Obstetrics & Gynecology, 1999. **93**(1): p. 135-139.

[18] Boppart, S.A., et al., High-resolution optical coherence tomography-guided laser ablation of surgical tissue. Journal of Surgical Research, 1999. **82**(2): p. 275-284.

[19] Boppart, S., et al., Forward-imaging instruments for optical coherence tomography. Optics letters, 1997. **22**(21): p. 1618-1620.

[20] Puliafito, C.A., et al., Imaging of macular diseases with optical coherence tomography. Ophthalmology, 1995. **102**(2): p. 217-229.

[21] Hee, M.R., et al., Optical coherence tomography of the human retina. Archives of ophthalmology, 1995. **113**(3): p. 325-332.

[22] Schuman, J.S., et al., Optical coherence tomography: a new tool for glaucoma diagnosis. Current opinion in ophthalmology, 1995. **6**(2): p. 89-95.

[23] Drexler, W., et al., In vivo ultrahigh-resolution optical coherence tomography. Optics letters, 1999. **24**(17): p. 1221-1223.

[24] Wojtkowski, M., et al., In vivo human retinal imaging by Fourier domain optical coherence tomography. Journal of biomedical optics, 2002. **7**(3): p. 457-463.

[25] Wojtkowski, M., et al., Three-dimensional retinal imaging with high-speed ultrahigh-resolution optical coherence tomography. Ophthalmology, 2005. **112**(10): p. 1734-1746.

[26] Zhang, J., B. Rao, and Z. Chen. Swept source based fourier domain functional optical coherence tomography. in 2005 IEEE Engineering in Medicine and Biology 27th Annual Conference. 2005.

[27] Drexler, W., et al., Ultrahigh-resolution ophthalmic optical coherence tomography. Nature medicine, 2001. **7**(4): p. 502-507.

[28] Yun, S., et al., Pulsed-source and swept-source spectral-domain optical coherence tomography with reduced motion artifacts. Optics Express, 2004. **12**(23): p. 5614-5624.

[29] Potsaid, B., et al., Ultrahigh speed spectral/Fourier domain OCT ophthalmic imaging at 70,000 to 312,500 axial scans per second. Optics express, 2008. **16**(19): p. 15149-15169.

[30] Srinivasan, V.J., et al., Ultrahigh-speed optical coherence tomography for three-dimensional and en face imaging of the retina and optic nerve head. Investigative ophthalmology & visual science, 2008. **49**(11): p. 5103.

[31] Grajciar, B. and O. Ondráček, Dispersion compensation in spectral domain optical coherence tomography.

[32] Aleksandrov, S., K. Subkhash, and M. Likhi, Nanosensitive optical coherence tomography for the study of changes in static and dynamic structures. Quantum Electronics, 2014. **44**(7): p. 657.

[33] Liu, Y., et al., Investigation of nanoscale structural alterations of cell nucleus as an early sign of cancer. BMC biophysics, 2014. **7**(1): p. 1.

[34] Alexandrov, S.A., et al., Synthetic aperture Fourier holographic optical microscopy. Physical review letters, 2006. **97**(16): p. 168102.

[35] Alexandrov, S.A., T.R. Hillman, and D.D. Sampson, Spatially resolved Fourier holographic light scattering angular spectroscopy. Optics letters, 2005. **30**(24): p. 3305-3307.

[36] Graf, R.N. and A. Wax. Nuclear morphology measurements using Fourier domain low-coherence interferometry. in Biomedical Optics 2005. 2005. International Society for Optics and Photonics.

[37] Robles, F., R.N. Graf, and A. Wax, Dual window method for processing spectroscopic optical coherence tomography signals with simultaneously high spectral and temporal resolution. Optics express, 2009. **17**(8): p. 6799-6812.

[38] Ralston, T.S., et al., Interferometric synthetic aperture microscopy. Nature Physics, 2007. **3**(2): p. 129-134.

[39] Wang, R.K. and A.L. Nuttall, Phase-sensitive optical coherence tomography imaging of the tissue motion within the organ of Corti at a subnanometer scale: a preliminary study. Journal of biomedical optics, 2010. **15**(5): p. 056005-056005-9.

[40] Choi, W., et al., Phase-sensitive swept-source optical coherence tomography imaging of the human retina with a vertical cavity surface-emitting laser light source. Optics letters, 2013. **38**(3): p. 338-340.

[41] Yi, J., et al., Can OCT be sensitive to nanoscale structural alterations in biological tissue? Optics express, 2013. **21**(7): p. 9043-9059.

[42] Alexandrov, S.A., et al., Spectral encoding of spatial frequency approach for characterization of nanoscale structures. Applied physics letters, 2012. **101**(3): p. 033702.

[43] Alexandrov, S.A., et al., Nano-sensitive optical coherence tomography. Nanoscale, 2014. **6**(7): p. 3545-3549.

[44] Born, M. and E. Wolf, Principles of optics: electromagnetic theory of propagation, interference and diffraction of light1999: Cambridge university press.

[45] Uttam, S., et al., Tomographic imaging via spectral encoding of spatial frequency. Optics express, 2013. **21**(6): p. 7488-7504.